Vortex-induced vibrations of a long flexible cylinder in shear flow

J. Fluid Mech. (2011), *vol.* 677, *pp.* 342–382.
doi:10.1017/jfm.2011.90

Vortex-induced vibrations of a long flexible cylinder in shear flow

REMI BOURGUET[1]†, GEORGE E. KARNIADAKIS[2] AND MICHAEL S. TRIANTAFYLLOU[1]

[1]Department of Mechanical Engineering, Massachusetts Institute of Technology, Cambridge, MA 02139, USA

[2]Division of Applied Mathematics, Brown University, Providence, RI 02912, USA

(Received 18 June 2010; revised 11 December 2010; accepted 15 February 2011; first published online 27 April 2011)

We investigate the in-line and cross-flow vortex-induced vibrations of a long cylindrical tensioned beam, with length to diameter ratio $L/D = 200$, placed within a linearly sheared oncoming flow, using three-dimensional direct numerical simulation. The study is conducted at three Reynolds numbers, from 110 to 1100 based on maximum velocity, so as to include the transition to turbulence in the wake. The selected tension and bending stiffness lead to high-wavenumber vibrations, similar to those encountered in long ocean structures. The resulting vortex-induced vibrations consist of a mixture of standing and travelling wave patterns in both the in-line and cross-flow directions; the travelling wave component is preferentially oriented from high to low velocity regions. The in-line and cross-flow vibrations have a frequency ratio approximately equal to 2. Lock-in, the phenomenon of self-excited vibrations accompanied by synchronization between the vortex shedding and cross-flow vibration frequencies, occurs in the high-velocity region, extending across 30 % or more of the beam length. The occurrence of lock-in disrupts the spanwise regularity of the cellular patterns observed in the wake of stationary cylinders in shear flow. The wake exhibits an oblique vortex shedding pattern, inclined in the direction of the travelling wave component of the cylinder vibrations. Vortex splittings occur between spanwise cells of constant vortex shedding frequency. The flow excites the cylinder under the lock-in condition with a preferential in-line versus cross-flow motion phase difference corresponding to counter-clockwise, figure-eight orbits; but it damps cylinder vibrations in the non-lock-in region. Both mono-frequency and multi-frequency responses may be excited. In the case of multi-frequency response and within the lock-in region, the wake can lock in to different frequencies at various spanwise locations; however, lock-in is a locally mono-frequency event, and hence the flow supplies energy to the structure mainly at the local lock-in frequency.

Key words: flow–structure interactions, vortex shedding, vortex streets

1. Introduction

Vortex-induced vibrations (VIV) of long flexible structures with bluff cross-sections are encountered in a great variety of physical problems, from the aeolian vibrations of hanging strings in air, to the vibrations of cables and risers placed within ocean

† Email address for correspondence: bourguet@mit.edu

currents. The possible fatigue damage resulting from VIV on these structures and the significantly increased drag forces require a careful calculation and prediction of the responses, and often the use of vortex-suppressing devices.

The simpler problem of a finite-span circular rigid cylinder, placed within a uniform flow, allowed to vibrate in the cross-flow direction only, has become the canonical problem of flow–structure interactions. The dual problems of a flexibly mounted cylinder free to vibrate in a cross-flow, and a cylinder forced to move harmonically at a prescribed frequency and amplitude, have shed light on the principal VIV mechanisms (Bearman 1984; Sarpkaya 2004; Williamson & Govardhan 2004). Large-amplitude, self-excited oscillations of flexibly mounted cylinders are observed when the vortex shedding frequency is synchronized with the structural cross-flow vibration, a condition referred to as 'lock-in'. Lock-in can occur over a range of oncoming flow velocities, and the vortex shedding frequency can be driven relatively far from the Strouhal frequency. The analysis of the vortex shedding pattern in the wake of oscillating rigid cylinders revealed the existence of different shedding modes associated with distinct regions of the synchronized regime (Williamson & Roshko 1988; Jauvtis & Williamson 2004; Dahl *et al.* 2007). These different vortex shedding modes have been related to significant changes of the fluid forces exerted on the body.

For a cylinder allowed to move in the in-line and cross-flow directions, significant differences were noted, because the shedding patterns are altered, and hence the forces and the overall response of the structure differ substantially relative to a cylinder vibrating in the cross-flow direction only (Sarpkaya 1995; Jeon & Gharib 2001; Jauvtis & Williamson 2004). In particular, the phase difference between in-line and cross-flow vibrations can have a strong influence on the regularity of the cylinder trajectory as well as on the possible occurrence of large high harmonics in the lift force (Jauvtis & Williamson 2004; Dahl *et al.* 2007, 2010).

For stationary long rigid cylinders, which either have a constant diameter and are placed in a sheared flow, or have a varying diameter and are placed in a uniform flow, the wake forms a cellular pattern composed of spanwise regions each with a different vortex shedding frequency (e.g. Gaster 1969, 1971; Griffin 1985; Peltzer & Rooney 1985; Noack, Ohle & Eckelmann 1991; Piccirillo & Van Atta 1993; Kappler *et al.* 2005). This cellular pattern is accompanied by an oblique orientation of the vortex rows, and vortex splittings between cells, similar to the vortex dislocations observed by Williamson (1992).

The investigation of the wake of rigid cylinders oscillating in the cross-flow direction in shear flow revealed the occurrence of lock-in on large spanwise cells; the cell length increased with the amplitude of vibration (Stansby 1976). For long tapered and pivoted cylinders in uniform flows, Techet, Hover & Triantafyllou (1998) and Flemming & Williamson (2005) reported the formation of a hybrid shedding mode composed of two distinct vortex shedding modes connected with a vortex split.

There are considerably fewer publications for the case of long flexible cylinders. Brika & Laneville (1993) studied a flexible cylinder in uniform flow, vibrating in its first mode in the cross-flow direction. They showed the existence of different vortex shedding modes at lock-in, similar to those observed behind rigid cylinders. Peltzer & Rooney (1985) studied the wake of a cable forced to oscillate in the cross-flow direction within a linearly sheared flow. As in the case of an oscillating rigid cylinder (Stansby 1976), increasing the amplitude of vibration induces a larger spanwise lock-in region.

Field and laboratory experiments on long flexible cylinders in sheared currents highlighted the mixed nature of the vibrations, involving high structural wavenumbers

and, often, multiple frequencies of response (e.g. Trim *et al.* 2005; Lie & Kaasen 2006; Jaiswal & Vandiver 2007; Vandiver, Jaiswal & Jhingran 2009). These studies have mainly focused on the quantification of the structure response but did not provide information concerning the localization and extent of the lock-in region or regarding the vortical patterns in the wake. Chaplin *et al.* (2005) and Huera-Huarte & Bearman (2009*a*) performed laboratory experiments on flexible cylinders in stepped currents. Chaplin *et al.* (2005) reported a range of excited wavenumbers in the in-line and cross-flow directions. For a flexible cylinder responding in its first structural mode in both the in-line and cross-flow directions, Huera-Huarte & Bearman (2009*a*,*b*) observed a well-defined synchronization between in-line and cross-flow motions at lock-in and reported much larger drag coefficients than those in the case of a stationary cylinder. Flow visualizations showed the occurrence of two distinct vortex shedding regimes depending on the vibration amplitude, as observed previously by Techet *et al.* (1998) and Flemming & Williamson (2005) for rigid cylinders under varying spanwise conditions.

Few numerical studies have been carried out on the VIV of flexible cylinders. Facchinetti, de Langre & Biolley (2004), Mathelin & de Langre (2005) and Violette, de Langre & Szydlowski (2007) modelled the fluid excitation by means of an empirical representation of the flow through a distribution of wake oscillators. They reported good agreement of this model with direct numerical simulation predictions. By means of direct numerical simulations, Newman & Karniadakis (1997) and Evangelinos & Karniadakis (1999) examined the VIV of a cylinder of aspect ratio 4π in uniform flow, at Reynolds numbers 100, 200 and 1000. These works provided a detailed analysis of the wake pattern and revealed the influence of the nature of the vibration (standing or travelling wave) on the vortical structure development. In these studies, lock-in was observed along the entire span. The influence of the Reynolds number on vibration amplitudes has been emphasized by Evangelinos & Karniadakis (1999) who showed that cross-flow motions of approximately one cylinder diameter occur at a Reynolds number of 1000, compared to 0.5–0.6 diameters at a Reynolds number of 100. Newman & Karniadakis (1997) also considered a flexible cylinder of aspect ratio 100, allowed to oscillate in the cross-flow direction, under the effect of a shear oncoming flow with a maximum Reynolds number of 100. They reported a mixed standing–travelling wave response. The case of long flexible cylinders of aspect ratio larger than 500, allowed to oscillate in the cross-flow direction only, and submitted to shear flows, has been investigated by Lucor, Imas & Karniadakis (2001) and Lucor, Mukundan & Triantafyllou (2006) at a Reynolds number of 1000 by means of low-resolution direct numerical simulations. In a linear shear flow, Lucor *et al.* (2001) reported a region of lock-in located in the high-velocity zone. Lucor *et al.* (2006) compared the cross-flow vibrations induced by linear and exponential shear flows and identified, in particular, a larger vibration bandwidth in the latter case. No analysis concerning the wake pattern and fluid–structure energy exchange was provided in this work.

Hence, when we consider long structures in shear flows, it is unclear whether the hydrodynamic data and even the insight from short-span rigid cylinders are applicable, and what new phenomena may appear. For this reason, in the present work we study the VIV of a flexible tensioned beam of aspect ratio 200, pinned at both ends and free to move in both the in-line and cross-flow directions under the effect of a linear shear flow. We employ direct numerical simulation in the range of Reynolds numbers of 110–1100. The structural parameters are chosen such that high-wavenumber vibrations similar to those observed in the laboratory and field experiments of Trim *et al.* (2005) and Vandiver *et al.* (2009), for example, are excited.

A joint analysis of the cylinder response and the vortical wake patterns is presented on the basis of high-resolution simulations.

The paper is organized as follows. The physical fluid–structure model and the numerical method are presented in § 2. The cylinder vibrations are examined in § 3. The mechanisms of the coupled fluid–structure system are investigated in § 4. The main findings of the present work are summarized in § 5.

2. Direct numerical simulation of the flow past a flexible cylinder

The three-dimensional flow past a flexible cylinder placed in sheared oncoming cross-flow is predicted using the direct numerical simulation of the incompressible Navier–Stokes equations. The cylinder has circular cross-section and is submitted to an oncoming flow which is everywhere parallel to the global x-axis and is linearly sheared along the global z-axis.

In the following, all physical variables are non-dimensionalized using the cylinder diameter D and the maximum inflow velocity U, which occurs at $z=0$. The non-dimensional time variable is denoted by t. The Reynolds number (Re) is based on D and the inflow velocity. The flow shear parameter is defined as $\beta=(1/U_a)\partial U_l/\partial z$, where U_l and U_a are the local and span-averaged non-dimensional oncoming flow velocities. The ratio between the maximum and the minimum inflow velocities is equal to 3.67 which leads to a value of the shear parameter ($\beta=0.006$) comparable to the experimental work of Peltzer & Rooney (1985) concerning stationary and flexible cylinders in a linear shear flow. Three Reynolds number ranges are considered: $Re\in$ [30, 110], $Re\in$ [90, 330] and $Re\in$ [300, 1100]; the minimum and maximum Re values are based on the minimum and maximum inflow velocities, respectively, while the three corresponding simulations are denoted by the maximum Reynolds number Re_m ($Re_m \in \{110, 330, 1100\}$).

The cylinder structure is modelled as an extensible tensioned beam; it has an aspect ratio of $L/D=200$, where L is the cylinder length in its equilibrium position in quiescent flow, it is pinned at both ends, while it is free to move in both the in-line (x) and cross-flow (y) directions. The cylinder mass ratio is defined as $m=\rho_c/\rho_f D^2$, where ρ_c is the cylinder mass per unit length, and ρ_f is the fluid density (Newman & Karniadakis 1997). The actual ratio between the mass of the cylinder and the mass of the displaced fluid is equal to $4m/\pi$. For the simulations herein, m is set equal to 6. The tension, bending stiffness and damping of the structure, designated by T, EI and K, respectively, are kept constant for the three simulations. The in-line and cross-flow displacements of the cylinder are denoted by ζ_x and ζ_y, respectively. The total drag and lift coefficients, including both pressure and viscous contributions, are denoted by C_x and C_y, respectively. The influence of gravity is neglected. The structural dynamics are governed by a tensioned beam model, expressed as follows in non-dimensional formulation:

$$\frac{\partial^2 \boldsymbol{\zeta}}{\delta t^2} - \omega_c^2 \frac{\partial^2 \boldsymbol{\zeta}}{\delta z^2} + \omega_b^2 \frac{\partial^4 \boldsymbol{\zeta}}{\delta z^4} + \frac{K}{m}\frac{\partial \boldsymbol{\zeta}}{\delta t} = \frac{1}{2}\frac{\boldsymbol{C}}{m}, \tag{2.1}$$

where $\boldsymbol{\zeta}=[\zeta_x, \zeta_y]^{\mathrm{T}}$ and $\boldsymbol{C}=[C_x, C_y]^{\mathrm{T}}$. ω_c and ω_b are the cable and beam phase velocities, defined by $\omega_c^2=T/m$ and $\omega_b^2=EI/m$, respectively. The structural damping is set equal to zero ($K=0$) to allow maximum amplitude oscillations to develop. A tensioned beam is considered in this study with $\omega_c=4.55$ and $\omega_b=9.09$. As shown in § 3, these structural parameters lead to vibrations involving high structural wavenumbers, which are representative of configurations encountered in the context of ocean engineering.

The coupled fluid–structure system is solved by the parallelized code *Nektar*, based on the spectral/*hp* element method (Karniadakis & Sherwin 1999). The version of the code employs a hybrid scheme with Fourier expansion in the spanwise (z) direction and Jacobi–Galerkin formulation in the (x, y) planes. A boundary-fitted coordinate formulation is used to take into account the cylinder unsteady deformation. Details regarding time integration schemes and validation studies of the numerical method and parameters have been reported in Newman & Karniadakis (1997) and Evangelinos & Karniadakis (1999), which addressed similar physical configurations. The computational domain extends $50D$ downstream and $20D$ in front, above and below the cylinder. A two-dimensional grid of 2175 elements with polynomial order $p = 6$ or $p = 7$, depending on the Reynolds number, is used in the (x, y) planes. In the z-direction, 512 planes (256 complex Fourier modes) are used for the $Re_m = 110$ case, and 1024 planes (512 complex Fourier modes) in the $Re_m = 330$ and $Re_m = 1100$ cases. This leads to a spatial resolution similar to that in the study of Evangelinos & Karniadakis (1999) for a cylinder of aspect ratio $L/D = 4\pi$ constrained to oscillate in the cross-flow direction, at $Re = 1000$. The boundary conditions have been implemented as described in Newman & Karniadakis (1997). A no-slip condition is applied on the cylinder surface. Fourier expansion implies spanwise periodicity of the flow and structural properties, and of the imposed shear velocity profile. The technique first used by Lucor (2004) is adopted here, wherein the inflow velocity profile is adjusted to enforce periodicity in a buffer region. The details and numerical tests concerning the buffer region are reported in Appendix A. The buffer region is not presented in the following. Information concerning the computational resources used is given in Appendix B.

3. In-line and cross-flow vibrations in shear flow

The cylinder VIV are quantified and analysed in this section. The investigation of the nature of structural response in shear flow is a first step leading to the identification of the principal mechanisms of the coupled fluid–structure system. An overview of the main features of the structural response is presented in § 3.1. A spectral analysis is carried out in § 3.2, with an emphasis on responses involving multiple frequencies. Finally, the synchronization between in-line and cross-flow motions is investigated in § 3.3.

3.1. *Space–time evolutions and statistics*

The time-averaged in-line displacement of the cylinder is presented in figure 1(a) for the three different Reynolds numbers. The shear of the oncoming flow induces an asymmetric bending of the structure with respect to the midspan point. This is also noted in experimental studies concerning a cylinder submitted to a stepped current (Chaplin *et al.* 2005). The maximum in-line displacement occurs at 40 % of the span and corresponds approximately to 6 % of the cylinder length. The Reynolds number considered in the simulation has only a small influence on the in-line steady displacement (3 % of relative difference on the maximum displacement between the $Re_m = 110$ and $Re_m = 1100$ cases). The effect of structural in-line bending on the flow patterns is discussed in §§ 4.1 and 4.2. The spanwise evolution of the time-averaged drag coefficient $\bar{C}_d$ is plotted in figure 1(b). In these plots, the drag coefficient is normalized by the local inflow velocity. The time-averaged drag coefficient is influenced by structural motion, in particular by the cross-flow vibration pattern. When Re_m increases from 110 to 1100, a slight increase of the $\bar{C}_d$ local maxima can

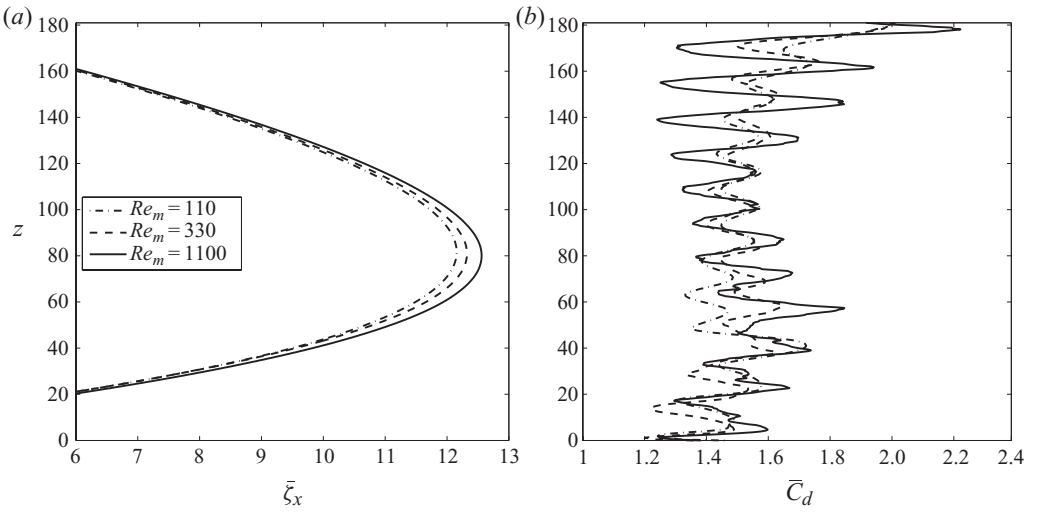

FIGURE 1. Time-averaged (*a*) in-line displacement and (*b*) drag coefficient, along the cylinder span.

be noticed in the region of maximum in-line displacement. Forces and fluid–structure energy transfer are investigated in § 4.3.

Selected time series of in-line and cross-flow motions, non-dimensionalized by D, are plotted along the cylinder span in figures 2 and 3. In these plots and in the following, only the deviations of the in-line motion from its mean value, $\tilde{\zeta}_x$, are shown.

A first review of the results raises several points: in both directions, the structural response is a combination of standing and travelling wave patterns as previously reported by Lucor *et al.* (2006) in the case of a long flexible cylinder constrained to oscillate in the cross-flow direction. The travelling character of these waves is preferentially oriented from high- to low-velocity regions (increasing z) and is more pronounced in the in-line direction. The structural displacements are not strictly periodic and transients can occur that perturb the spatio-temporal pattern of the response. Concerning the in-line motion, standing wave patterns strongly modulate the travelling waves near the ends, especially in the high-velocity region, for $0 < z < 20$ at $Re_m = 110$, and for $0 < z < 40$ at $Re_m = 330$. Beyond these regions, distinct travelling waves can be observed. cross-flow responses present more homogeneously mixed standing and travelling wave patterns along the span. The case $Re_m = 1100$ exhibits less pronounced travelling wave patterns in both directions. These points are further investigated quantitatively in the following.

Maximum and root mean square (r.m.s.) values of the structural response amplitudes along the cylinder span are presented in figure 4. Both maximum and r.m.s. values reflect the above-mentioned standing–travelling wave patterns. The standing character of the responses leads to the formation of cells along the span corresponding to alternating 'nodes' (minima of the response envelope) and 'anti-nodes' (maxima of the response envelope). Despite the shear flow, the displacements associated with 'anti-nodes' remain relatively constant along the cylinder span. This partitioning of the responses in spanwise cells is modulated by the superimposed travelling wave patterns. In particular, it appears that the r.m.s. values of displacements associated with 'nodes' are different from zero which indicates that these 'nodes' are moving

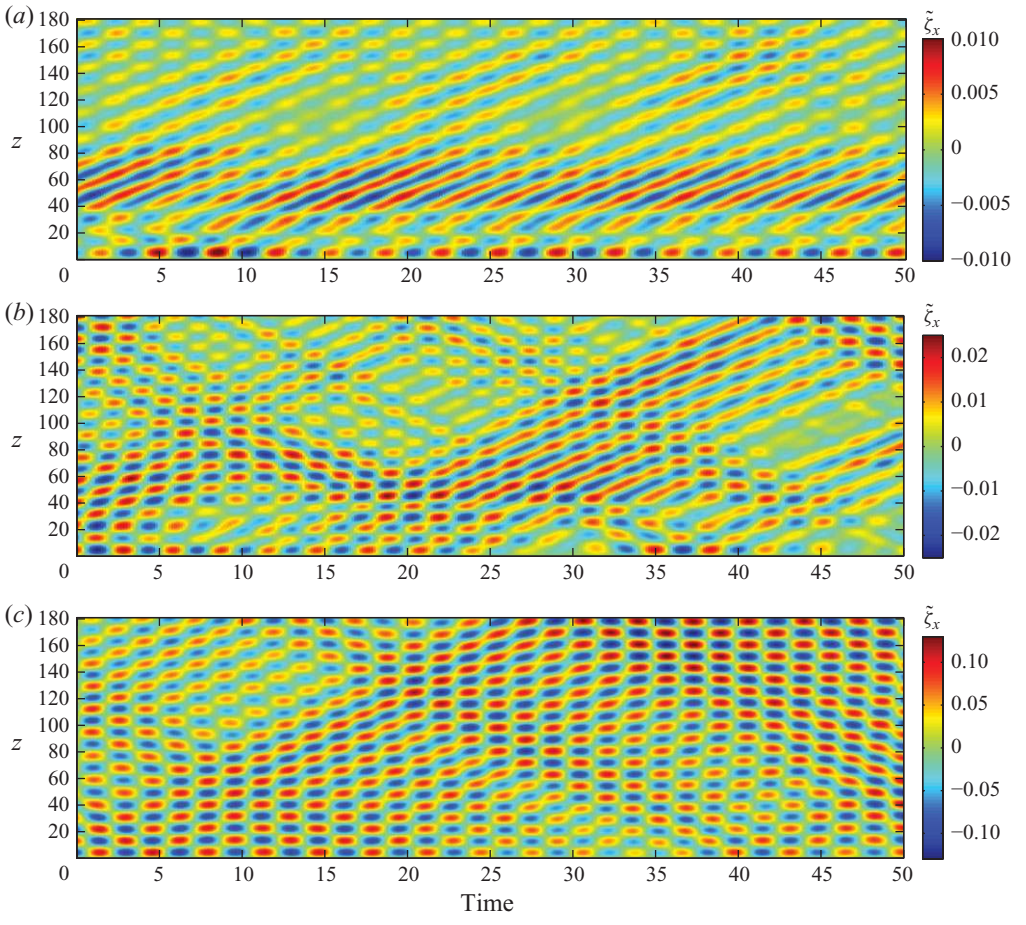

FIGURE 2. Temporal evolution of in-line displacement fluctuation along the cylinder span at (*a*) $Re_m = 110$, (*b*) $Re_m = 330$ and (*c*) $Re_m = 1100$.

due to the presence of travelling wave components. The dominant character of the travelling wave pattern on in-line displacements almost suppresses these standing wave cells on most of the cylinder span at $Re_m = 110$ and $Re_m = 330$.

The effect of the Reynolds number on response amplitudes had previously been reported by Evangelinos & Karniadakis (1999), concerning cross-flow vibrations in uniform flow. It can be observed that the Re_m influence appears more pronounced in the in-line direction and that the ratio between the cross-flow and the in-line maximum oscillation amplitudes decreases as Re_m increases. The Reynolds number effect on the structural response can partly be related to modifications occurring in the wake pattern as shown in § 4.2. The amplitudes of vibration observed at $Re_m = 1100$ are similar to those observed in the experimental measurements carried out with flexible cylinders at higher Reynolds numbers (Chaplin *et al.* 2005; Trim *et al.* 2005; Lie & Kaasen 2006; Huera-Huarte & Bearman 2009*a*). In a linear shear flow and for $Re_m \in [4800, 34\,200]$, Lie & Kaasen (2006) reported span-averaged r.m.s. values of the displacement in the range $0.05D$–$0.08D$ in the in-line direction and about $0.25D$ in the cross-flow direction. In the case of flexible cylinders constrained to oscillate in the cross-flow direction in a linear shear flow at $Re_m = 1000$, Lucor *et al.* (2001) and Lucor *et al.* (2006) reported span-averaged r.m.s. values of the displacement approximately

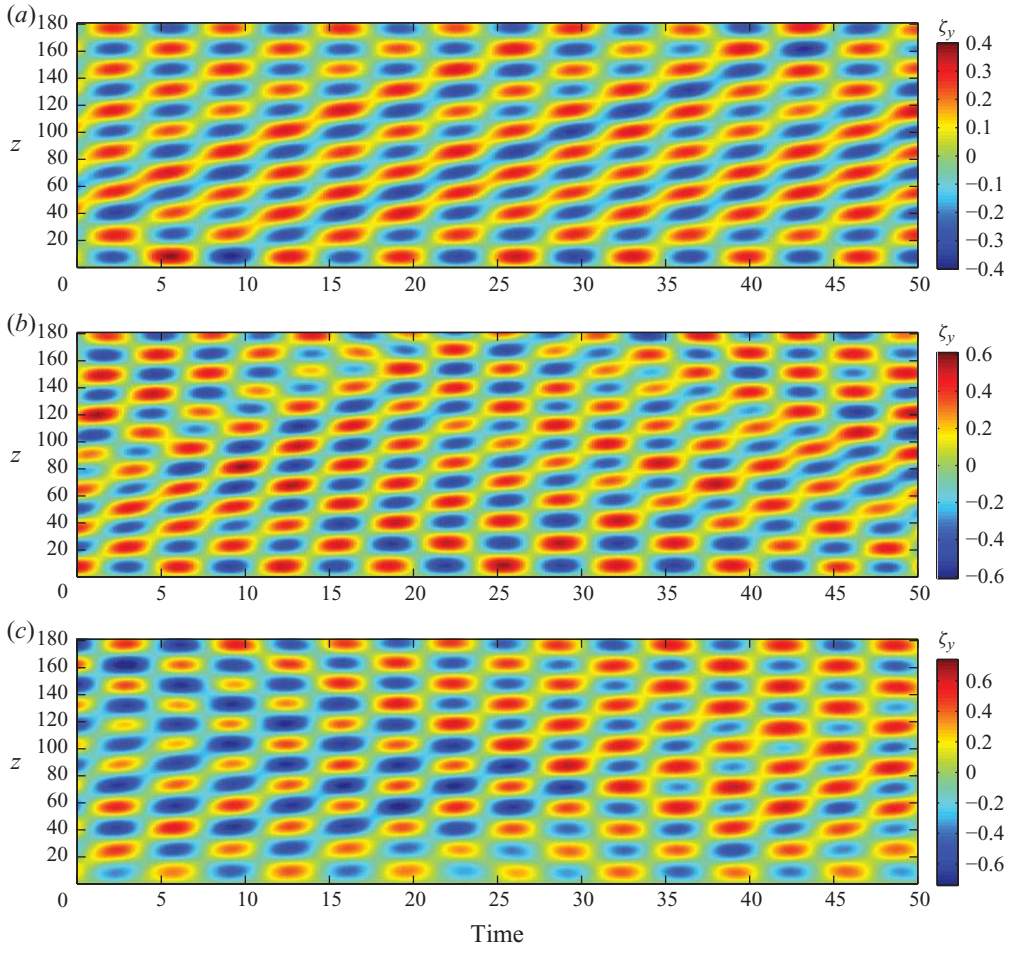

FIGURE 3. Temporal evolution of cross-flow displacement along the cylinder span at (*a*) $Re_m = 110$, (*b*) $Re_m = 330$ and (*c*) $Re_m = 1100$.

equal to $0.24D$ and $0.23D$ for low- and high-wavenumber vibrations, respectively. In the present case, $0.045D$ and $0.26D$ are reached in the in-line and cross-flow directions, at $Re_m = 1100$. Despite the influence of the Re_m on the amplitude of the vibrations, the basic mechanisms of the structural vibrations remain the same as the Reynolds number increases, as also discussed in the following.

3.2. *Spectral analysis of the structural response*

Spectral analysis is performed on the entire time series of the cylinder motions, after the initial transient dies out. The objective is to characterize the standing–travelling wave pattern of the structural response from both the temporal and spatial points of view. Spanwise distributions of the temporal power spectra of the in-line and cross-flow vibrations are presented in figures 5 (a, c, e) and 6 (a, c, e). In these plots, the power spectral densities (PSD) of ζ_x and ζ_y are normalized at each spanwise location by the corresponding displacement variance.

Concerning the in-line motion, a response at a single frequency is observed at $Re_m = 110$ along the entire span, while the cases $Re_m = 330$ and $Re_m = 1100$ exhibit

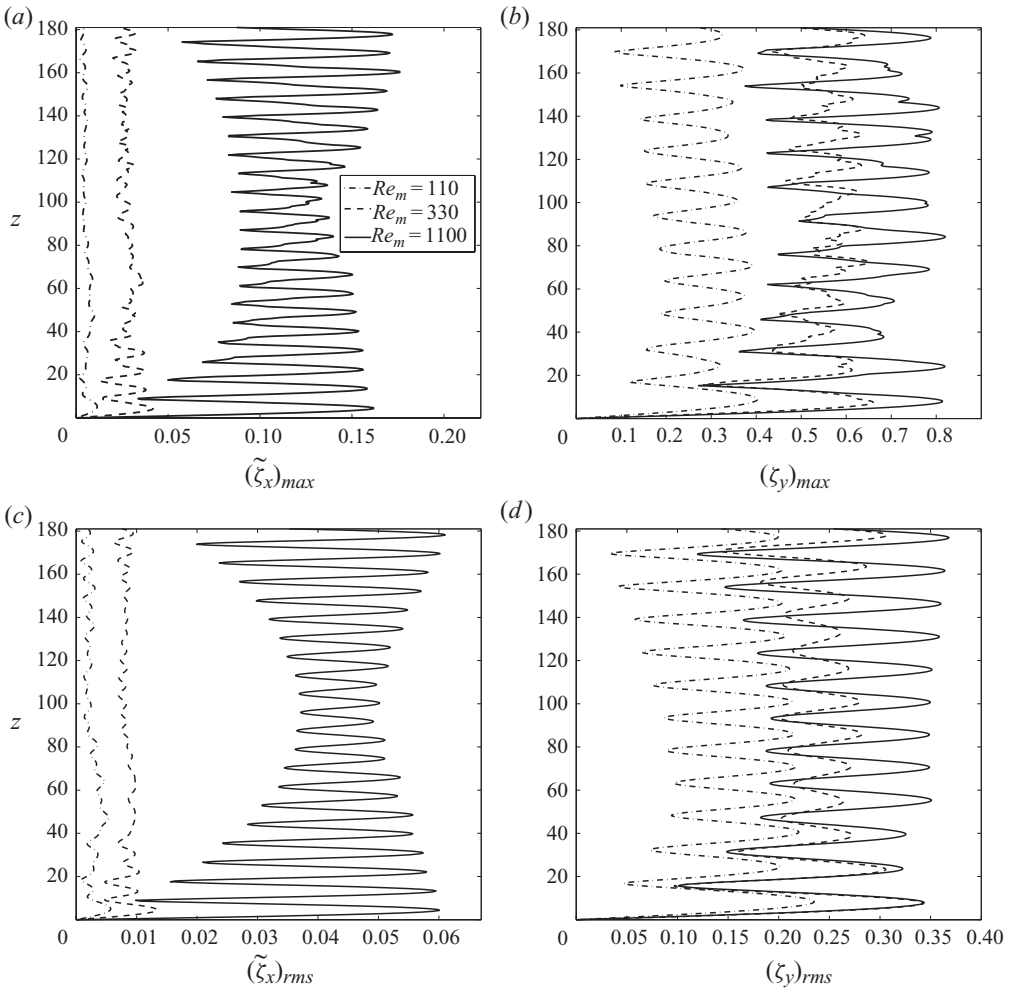

FIGURE 4. (a, b) Maximum and (c, d) r.m.s. values of (a, c) in-line displacement fluctuation and (b, d) cross-flow displacement along the cylinder span.

responses at several frequencies. These two types of responses are referred to herein as 'mono-frequency' and 'multi-frequency', respectively. The possible causes of a switch between mono- and multi-frequency responses, as Re_m is changed, are currently under investigation.

At $Re_m = 330$, four response frequencies of relatively similar amplitude are competing, while secondary peaks are also present. It can be observed that the peaks are clearly defined and distinct from each other, despite a narrow-band vibration, in the range of $[0.24, 0.36]$. The corresponding frequencies present spectral peaks along the entire span. This is also the case at $Re_m = 1100$ where a single spectral peak dominates among several response peaks. In all cases, the spanwise pattern of PSD exhibits well-defined cells that are related to the excitation of specific structural wavelengths, as shown in the following. The standing or travelling character of each excited temporal response is studied by means of a technique suggested by Lucor *et al.* (2006). Fourier series can be used to approximate the structure response as follows, using $N + 1$ temporal Fourier modes:

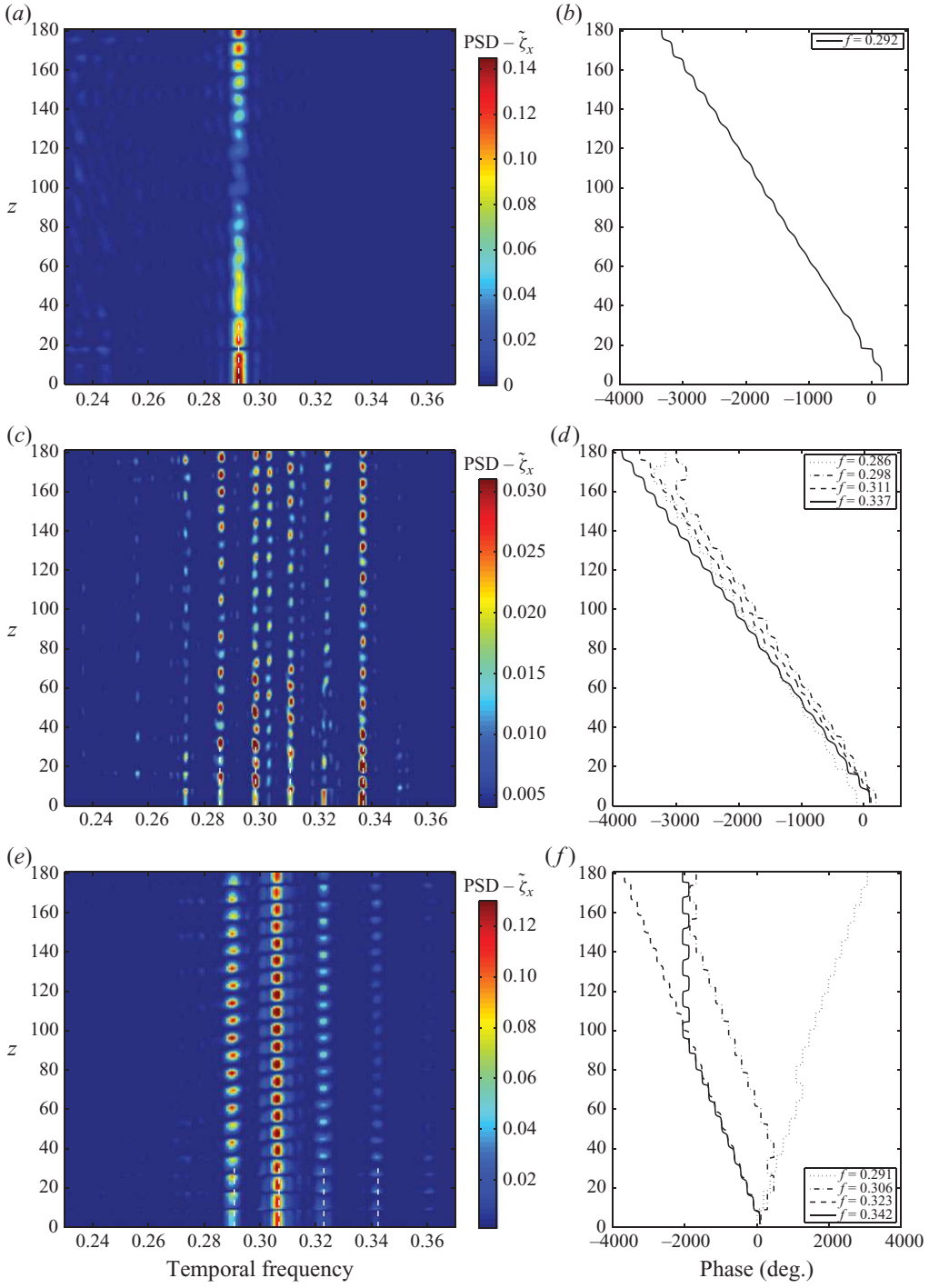

FIGURE 5. Temporal spectral analysis of in-line displacement fluctuation: (a,c,e) PSD of $\tilde{\zeta}_x$ along the cylinder span and (b,d,f) spanwise evolution of selected temporal mode phase angles at (a,b) $Re_m = 110$, (c,d) $Re_m = 330$ and (e,f) $Re_m = 1100$.

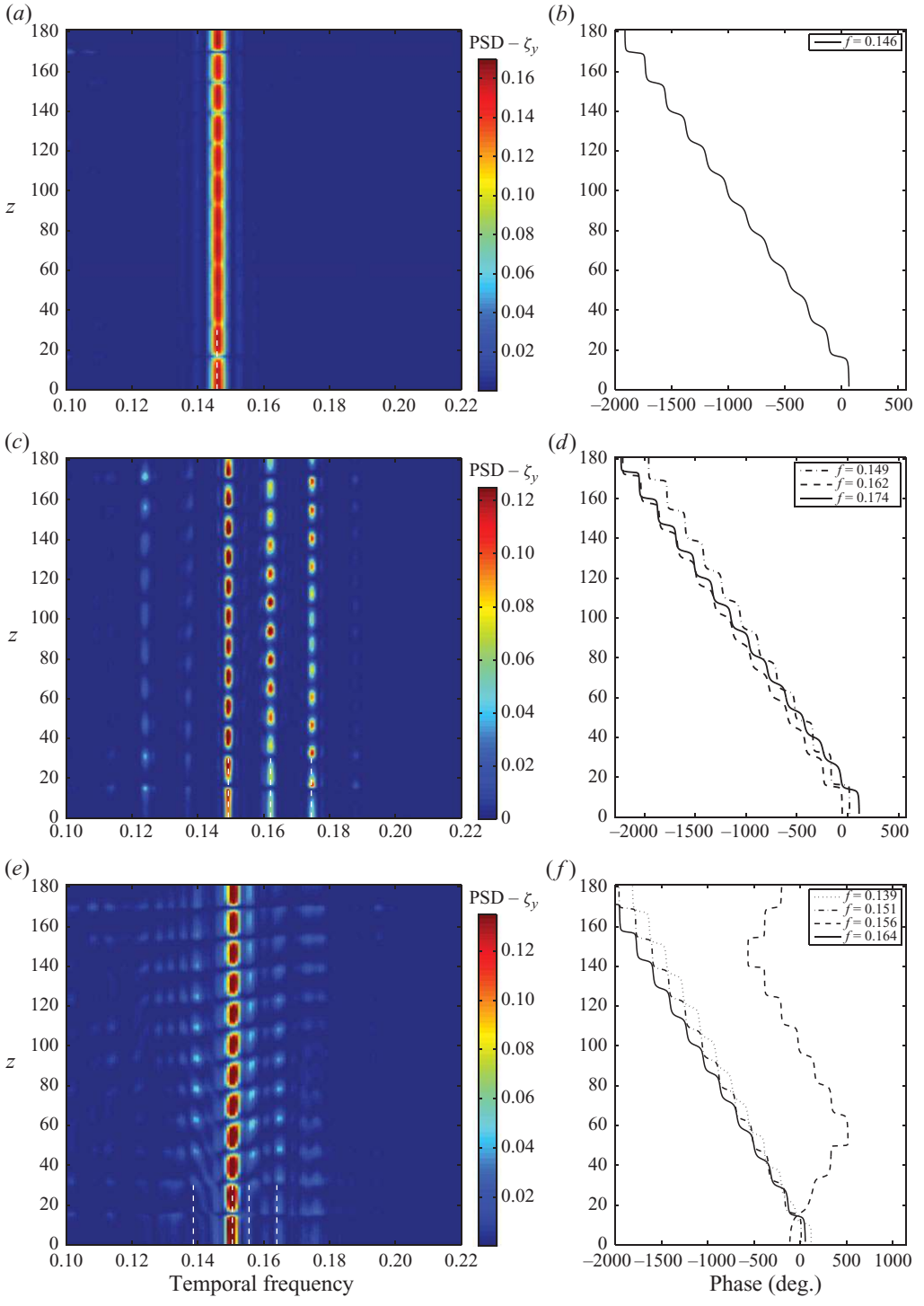

FIGURE 6. Temporal spectral analysis of cross-flow displacement: (a,c,e) PSD of ζ_y along the cylinder span and (b,d,f) spanwise evolution of selected temporal mode phase angles at (a,b) $Re_m = 110$, (c,d) $Re_m = 330$ and (e,f) $Re_m = 1100$.

$$\tilde{\zeta}_x(z,t) \approx \sum_{q=-N/2}^{N/2} a_q^x(z)\,\exp[2\pi \mathrm{i} f_q t] = \sum_{q=-N/2}^{N/2} |a_q^x|(z)\exp\left[\mathrm{i}\left(2\pi f_q t + \psi_q^x(z)\right)\right] \quad (3.1)$$

$$\zeta_y(z,t) \approx \sum_{q=-N/2}^{N/2} a_q^y(z)\,\exp[2\pi \mathrm{i} f_q t] = \sum_{q=-N/2}^{N/2} |a_q^y|(z)\exp\left[\mathrm{i}\left(2\pi f_q t + \psi_q^y(z)\right)\right], \quad (3.2)$$

where $f_q = q/T_s$ is the frequency associated with the qth mode and T_s the sampling period. The complex modal coefficients a_q^x and a_q^y are also written in terms of their moduli ($|a_q^x|$ and $|a_q^y|$) and their spatial phase angles (ψ_q^x and ψ_q^y). The spanwise evolution of the phase angles are presented in figures 5 (b,d,f) and 6 (b,d,f), for the selected frequencies shown in figures 5 (a,c,e) and 6 (a,c,e), respectively, through dashed lines (lower part of the PSD plots); only positive frequencies ($q \in [0, N/2]$) are plotted. As a consequence, spatial phase angles which are decreasing along the span (increasing z) denote travelling waves oriented from high-velocity regions (near $z = 0$) towards the low-velocity regions; and vice versa for phase angle increasing along the span. At $Re_m = 110$ and $Re_m = 330$, the predominant frequencies of in-line vibration are associated with travelling waves moving towards the low-velocity regions.

Modulations can be noticed in the nearly linear evolution of the spatial phase angles. This saw-tooth or zigzagging evolution is due to the underlying standing wave pattern. In the idealized case of a strictly linear spatial phase variation (pure travelling wave), the total phase of the qth mode becomes $2\pi f_q t + 2\pi k_q^x z + \eta_q^x$. The slope of ψ_q^x can be used to determine the excited structural wavenumber k_q^x; η_q^x denotes a phase lag which is independent of z. Sine Fourier modes ($\sin(\pi n z D/L)$ for the nth mode) are often used to describe the structural response (e.g. Chaplin *et al.* 2005; Lie & Kaasen 2006). For illustration purposes, and comparison with the existing literature, the excited wavenumber k_q^x can be related to the sine Fourier mode $2k_q^x(L/D)$. In the case $Re_m = 110$, a linear approximation of ψ_q^x indicates that the excited wavenumber corresponds to the 22nd structural mode, which is also verified in the following by a joint space/time spectral analysis. The in-line response is more complex at $Re_m = 1100$.

A similar analysis is carried out for cross-flow vibrations (figure 6). At $Re_m = 110$, a single frequency is excited along the span and corresponds to a wave travelling towards low-velocity regions. The case $Re_m = 330$ exhibits a multi-frequency response with three frequencies emerging; they are all related to waves travelling towards the low-velocity region. For free vibrations in the cross-flow direction only, Lucor *et al.* (2006) also reported three excited frequencies associated with waves travelling in the same direction, in a linear shear flow. The wave associated with a wider predominant peak at $Re_m = 1100$ is also travelling towards the low-velocity region. The wave corresponding to one of the secondary peaks is travelling towards $z = 0$ near the ends.

The ratio between in-line and cross-flow predominant frequencies is very close to 2 at $Re_m = 110$. In the case $Re_m = 330$, the predominant frequency in the cross-flow direction (0.149) can be linked to the peak occurring at 0.298 in the in-line direction, leading to a ratio of 2. The second cross-flow frequency (0.162) is associated through a ratio of 2 with secondary in-line peaks. The third cross-flow frequency (0.174) can be linked to a very small in-line contribution around 0.35, that can be identified for $z < 40$. The frequency ratio of in-line and cross-flow predominant frequencies is equal to 2.03 at $Re_m = 1100$. This apparent slight deviation from 2 is due to irregularities occurring in the instantaneous excited frequencies, in both directions.

In order to relate the excited frequencies to structural wavenumbers, a spatio-temporal spectral analysis based on a two-dimensional fast Fourier transform of the evolution of structural responses is performed. In figure 7, two-dimensional PSD of in-line and cross-flow motions are plotted as functions of frequency and spatial wavenumber. Positive frequencies are presented and thus negative wavenumbers (upper part of each plot) are associated with travelling waves moving towards low-velocity regions, while positive wavenumbers (lower part of each plot) represent travelling waves moving towards high-velocity regions. The PSD is normalized by the maximum value observed in both domains (positive and negative wavenumbers). The frequencies identified in figures 5 and 6 are indicated by white vertical dashed lines in the corresponding plots. For comparison purposes, selected sine Fourier mode wavenumbers are indicated by yellow horizontal dashed lines.

The predominant excited wavenumbers correspond to modes $n \in \{22, 23, 24, 25\}$ in the in-line direction and $n \in \{13, 14, 15\}$ in the cross-flow direction. These mode numbers are close to those measured experimentally by Trim *et al.* (2005) and Lie & Kaasen (2006), where cases of multi-frequency response have been reported in shear flow. It is recalled that in the present case of mixed standing–travelling wave responses, the concept of structural modes and the association of the excited wavenumbers with the corresponding sine Fourier modes are used loosely, for illustration purposes only. The proximity of the contributions of wavenumbers ± 0.0325 and ± 0.035 in the case $Re_m = 330$ (cross-flow) is in agreement with the fact that 12 or 13 nodes can be observed alternatively in the response pattern.

In all cases, the ratio between the in-line and cross-flow excited wavenumbers is different from 2 as expected, since for a mixed cable/beam structure, the relation between a spatial wavenumber and the corresponding natural frequency is not linear (see expression (3.3) in the following). As a consequence, the nodes of standing wave pattern in the cross-flow direction do not necessarily coincide with in-line motion nodes. This creates a perturbation of the in-line/cross-flow motion synchronization pattern as explained in § 3.3.

In general, at a given vibration frequency it appears that only a single peak emerges in the spatial spectrum, at the same wavenumber on both the negative and positive sides; i.e. a single structural wavelength is excited at a given frequency. Conversely, a given spatial wavelength responds mainly to a single frequency that depends on Re_m. Exceptions exist, as for instance in the case $Re_m = 330$, where the wavenumber 0.0575 is excited at two distinct frequencies in the in-line direction. As expected, the excited structural wavenumber increases with increasing excitation frequency. The natural frequency f^{nat} of the tensioned beam associated with the wavenumber k can be evaluated as follows, in vacuum:

$$f^{nat}(k) = k\sqrt{\omega_c^2 + 4\pi^2\omega_b^2 k^2}. \tag{3.3}$$

The frequencies corresponding to the selected wavenumbers are indicated by white crosses in figure 7. The effective vibration frequencies present a strong drift from the natural frequency spectrum. This spectrum can be modified as follows to take into account the immersion of the cylinder into the fluid:

$$f^{mod} = f^{nat}\sqrt{\frac{m}{m + \dfrac{\pi}{4}C_m}}, \tag{3.4}$$

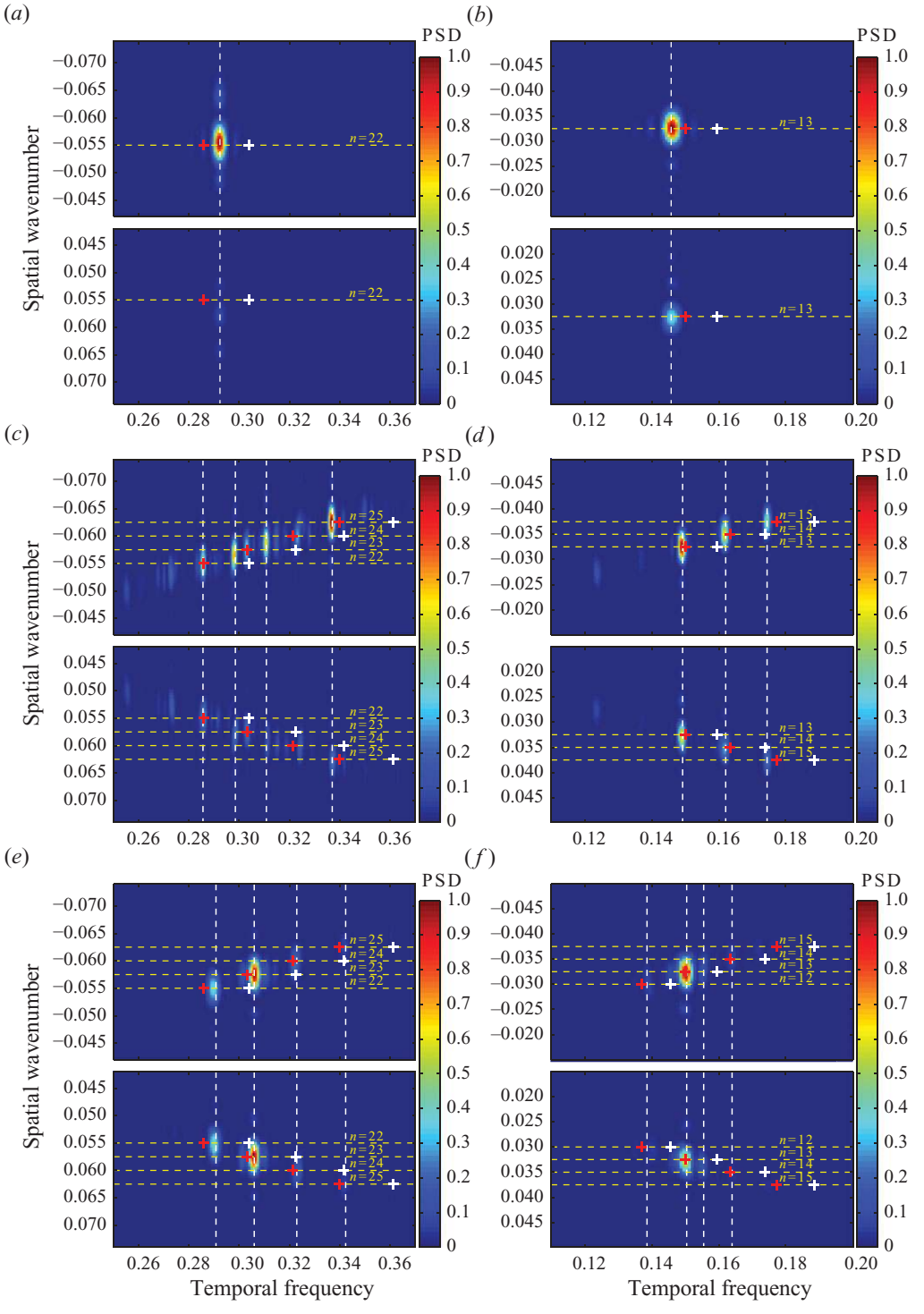

FIGURE 7. Spatio-temporal spectral analysis of (a,c,e) in-line displacement fluctuation and (b,d,f) cross-flow displacement at (a,b) $Re_m = 110$, (c,d) $Re_m = 330$ and (e,f) $Re_m = 1100$. The white vertical dashed lines denote the frequencies identified in figures 5 and 6. The wavenumbers of selected sine Fourier modes are indicated by yellow horizontal dashed lines. The white (red) crosses denote the natural (modified) frequencies associated with these wavenumbers.

where C_m is the added mass coefficient induced by the fluid. The corresponding modified frequencies f^{mod}, for a choice of $C_m = 1$, are indicated by red crosses in figure 7. While this modified spectrum seems to provide a reasonable approximation to the effective excited frequencies in some cases, significant discrepancies appear in other cases, as for example in both directions at $Re_m = 110$ and in the in-line direction at $Re_m = 1100$. This emphasizes the variability of the added mass coefficient and hence the difficulty of estimating *a priori* the structural response.

The relative weights of negative and positive wavenumber peaks for the same frequency confirm the observations made previously concerning the mixed standing–travelling character of structural vibrations and, especially, the reinforced standing character of the response at $Re_m = 1100$.

The spectral analysis demonstrates the existence of multi-frequency responses, where different structural wavenumbers are excited. At a given spanwise location, several structural wavenumbers can contribute significantly to the total vibration. This is the case at $Re_m = 330$ in the cross-flow direction, for instance (figure 6*c*). Since the three excited frequencies are associated with a distinct wavenumber, the distribution of nodes and anti-nodes along the span leads to three possible vibrating configurations, with one, two or three frequencies present at each spanwise location. It should be noted, again, that we are using the term 'node' loosely, to denote a minimum in the envelope of the response; it is not strictly speaking a node where the response is zero.

The question that arises is whether the response is instantaneously mono-frequency, with a shifting frequency in time, or it is multi-frequency at all times. This question is addressed by means of time/frequency analysis. At each spanwise location, the instantaneous frequency content of the response can be monitored as a function of time by computing a scalogram, which shows the squared magnitude of a continuous wavelet transform as a function of the frequency and time (Boashash 2003). Three different locations, that exhibit one-, two- and three-frequency responses, are selected along the span ($z = 94$, $z = 44$ and $z = 7.5$, respectively), and the corresponding time series and scalograms are plotted in figure 8 over a selected time interval. In these plots, the three predominant frequencies identified in the previous spectral analysis are indicated by dashed lines. The mono-frequency case (figure 8*a*) exhibits only small deviations about the predominant frequency. In both multi-frequency cases (figure 8*b*,*c*), the structural response does not exhibit an instantaneous broad spectrum; instead the vibration is instantaneously dominated by a single frequency, that drifts relatively regularly from one predominant frequency to another. As a consequence, the response previously identified as multi-frequency, because of its overall spectral content, can be regarded as 'instantaneously mono-frequency'. This observation is verified along the whole span and is also verified in the case of a multi-frequency response in the in-line direction, even though the scalograms are noisier in this case.

Figure 8 shows that the temporal variation of the dominant frequency does not occur simultaneously along the entire span. As a result, different structural wavenumbers can be excited instantaneously along the cylinder span. To illustrate this point, the instantaneous predominant frequency f_p is plotted as a function of time and space in figure 9. The three dashed lines indicate the location of the signals analysed in figure 8. This spatio-temporal map of the response frequency confirms that different frequencies, and thus structural wavenumbers, are excited simultaneously, but at different locations along the cylinder span. The distribution of excited frequencies resembles a low-frequency travelling wave with non-constant amplitude, as it is modulated by the standing-wave component of the structural

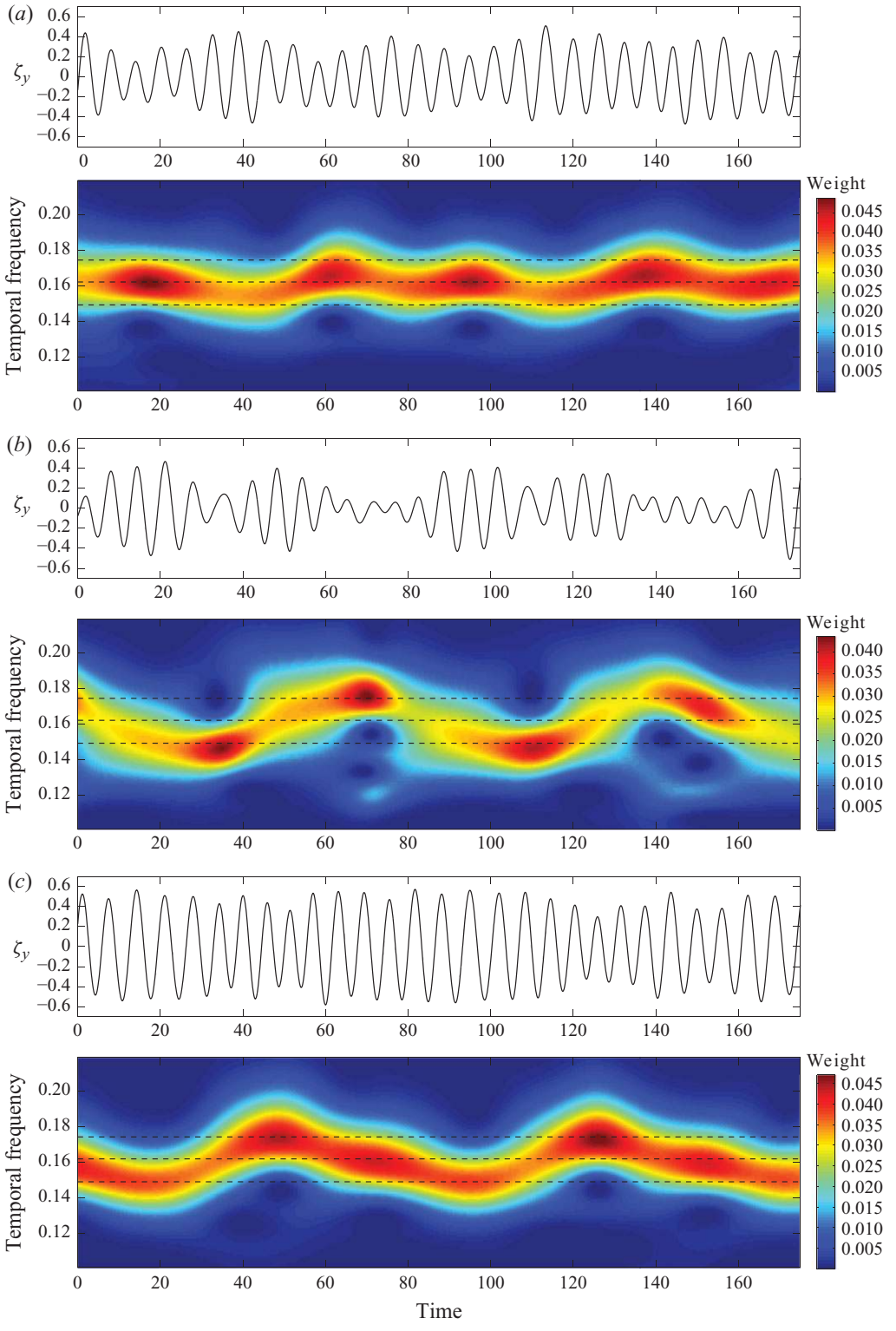

FIGURE 8. Selected cross-flow displacement time series (upper part) and corresponding frequency content as a function of time (scalogram, lower part) in the case $Re_m = 330$ at (*a*) $z = 94$, (*b*) $z = 44$ and (*c*) $z = 7.5$. The dashed lines denote the predominant frequencies identified in figure 6(*c*).

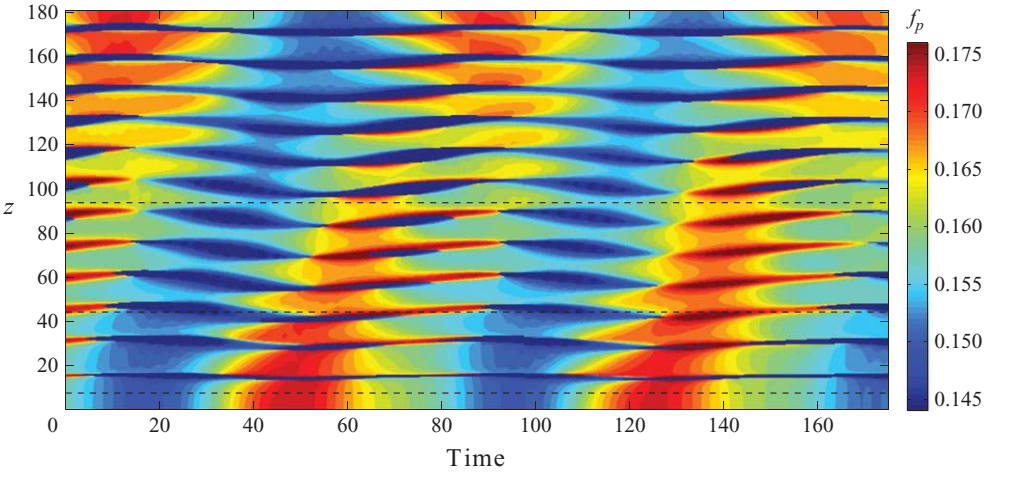

FIGURE 9. Predominant frequency of cross-flow displacement as a function of time along the cylinder span in the case $Re_m = 330$. The dashed lines indicate the time series presented in figure 8.

motion. In high (low) dominant frequency regions, the distance between two adjacent nodes tends to decrease (increase) leading to an undulated stripped pattern.

So far, in-line and cross-flow vibrations have been reported separately. They are, in fact, coupled nonlinearly via the flow forces, and hence an investigation of the synchronization between the in-line and cross-flow displacements is performed next to properly characterize the structural response.

3.3. *Synchronization of in-line and cross-flow vibrations*

The synchronization between the in-line and cross-flow displacements of an elastically mounted rigid cylinder has been investigated experimentally in Dahl *et al.* (2007) and Dahl *et al.* (2010). It was shown that there is a strong influence of the in-line versus cross-flow motion phase difference on the wake patterns and hence on the forces acting on the structure. Concerning long flexible cylinders in shear flows, Vandiver *et al.* (2009) and Modarres-Sadeghi *et al.* (2010) have emphasized, on the basis of experimental measurements, a possible link between this synchronization and the distribution of excitation and damping regions along the span.

The same phenomena are also addressed here in § 4.3. Synchronization is quantified in terms of the phase difference between in-line and cross-flow vibrations along the cylinder span and is shown to be related to the nature of the fluid–structure energy transfer. Selected cylinder trajectories at different spanwise locations are shown in figure 10. These Lissajous curves depict 'figure-eight' orbits, which often characterize in-line responses at approximately twice the cross-flow frequency. The phase difference between synchronized in-line and cross-flow motions controls the specific shape and direction of travel in these orbits.

The instantaneous phases of in-line and cross-flow vibrations (ϕ_x and ϕ_y respectively) are determined by means of the Hilbert transform. Adopting an approach similar to that in Huera-Huarte & Bearman (2009*a*), the phase difference Φ_{xy} is evaluated as follows:

$$\Phi_{xy} = [p\phi_x - q\phi_y, \mod 360^\circ], \tag{3.5}$$

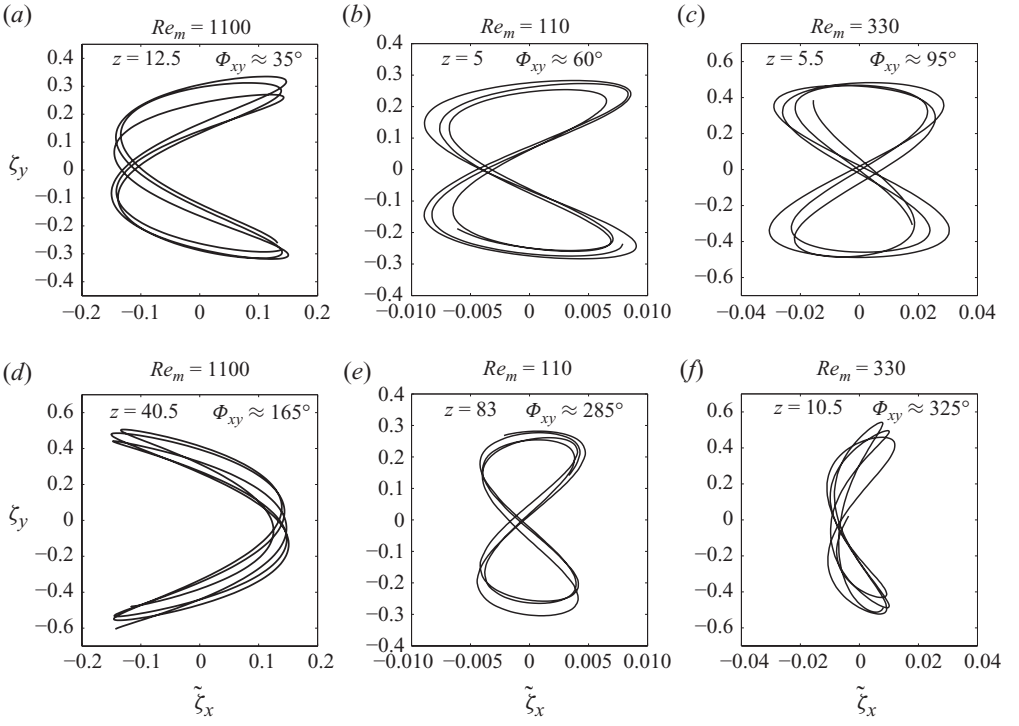

FIGURE 10. Selected trajectories of the cylinder at different spanwise locations in the three cases $Re_m = 110$, $Re_m = 330$ and $Re_m = 1100$.

where p and q are two integer numbers defining the level of synchronization. Considering the spectral analysis presented in § 3.2, the couple $(p, q) = (1, 2)$ is chosen here. Values of Φ_{xy} in the range 0°–180° (180°–360°, respectively) correspond to orbits where the cylinder moves upstream (downstream, respectively) when reaching the cross-flow oscillation maxima. These two types of trajectories are referred to as 'counter-clockwise' and 'clockwise', respectively (Dahl *et al.* 2007). Values of Φ_{xy} are specified for each trajectory in figure 10.

Spatio-temporal evolutions of the phase difference associated with the time series presented in figures 2 and 3 are plotted in figure 11. As previously mentioned in Huera-Huarte & Bearman (2009*a*), an analysis of the phase angle assumes that the in-line and cross-flow motions are synchronized over an extended time interval, i.e. the temporal evolution of Φ_{xy} exhibits plateaux. Such plateaux are observed for the three cases studied herein, as illustrated in figure 10. Figure 11 depicts for each case a horizontally stripped pattern with relatively regular jumps along the span. At a given spanwise location, the unsteadiness of phase difference increases with Re_m.

To quantify the predominant phase difference along the span, histograms of Φ_{xy} are evaluated from the entire time series. Figure 12 shows, for each Re_m and at each spanwise location, the relative weights of phase difference angles. The contributions are normalized by the maximum weight. Increasing unsteadiness of the phase difference leads to noisier histograms as Re_m increases. Despite this, a predominant phase difference can be identified in most cases.

At $Re_m = 110$, a first region can be distinguished for $z < 20$, approximately, where the spanwise evolution of the phase angle resembles that of standing waves in the

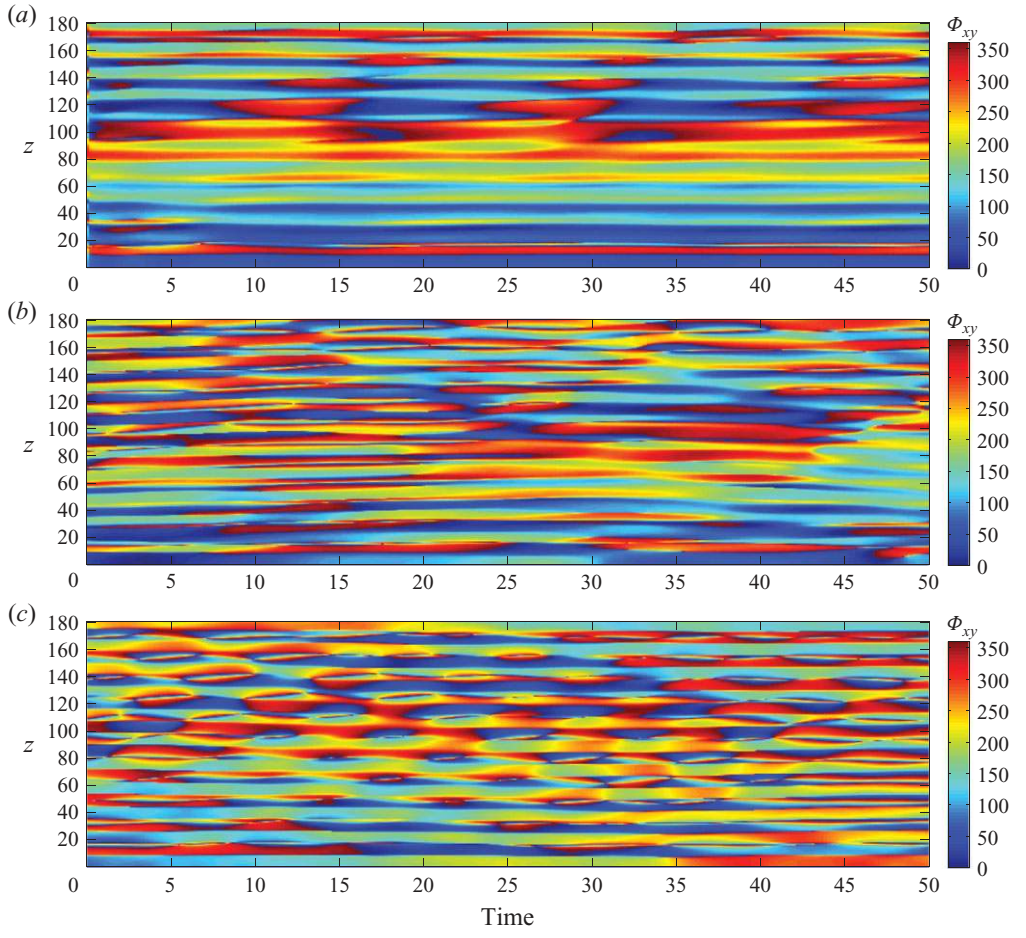

FIGURE 11. Temporal evolution of the phase difference between in-line and cross-flow displacements (3.5) along the cylinder span at (*a*) $Re_m = 110$, (*b*) $Re_m = 330$ and (*c*) $Re_m = 1100$.

in-line and cross-flow directions with the excited in-line structural mode corresponding to twice the cross-flow modal number. Indeed, in that case the anti-node of cross-flow displacement corresponds to a node of in-line displacement, where a change in orbit orientation also occurs. Here, $\Phi_{xy} \approx 60^\circ$ at $z = 5$ and $\Phi_{xy} \approx 300^\circ$ at $z = 14$.

A similar pattern can be identified in the case $Re_m = 330$, with a switch between clockwise and counter-clockwise trajectories. This is related to the predominant standing wave pattern in this region.

Note that the excited structural wavelength in the in-line direction is not exactly half of the cross-flow one, and the standing waves are perturbed by the development of travelling waves; this explains why the alternating clockwise/counter-clockwise pattern does not persist beyond this region.

In the idealized case of pure travelling waves in both directions, with double frequency in the in-line direction, a constant phase difference could be observed along the span. At $Re_m = 110$, the mixed standing–travelling wave patterns lead to a zigzagging distribution of Φ_{xy}. Jumps of $+130^\circ$ occur between cells defined by

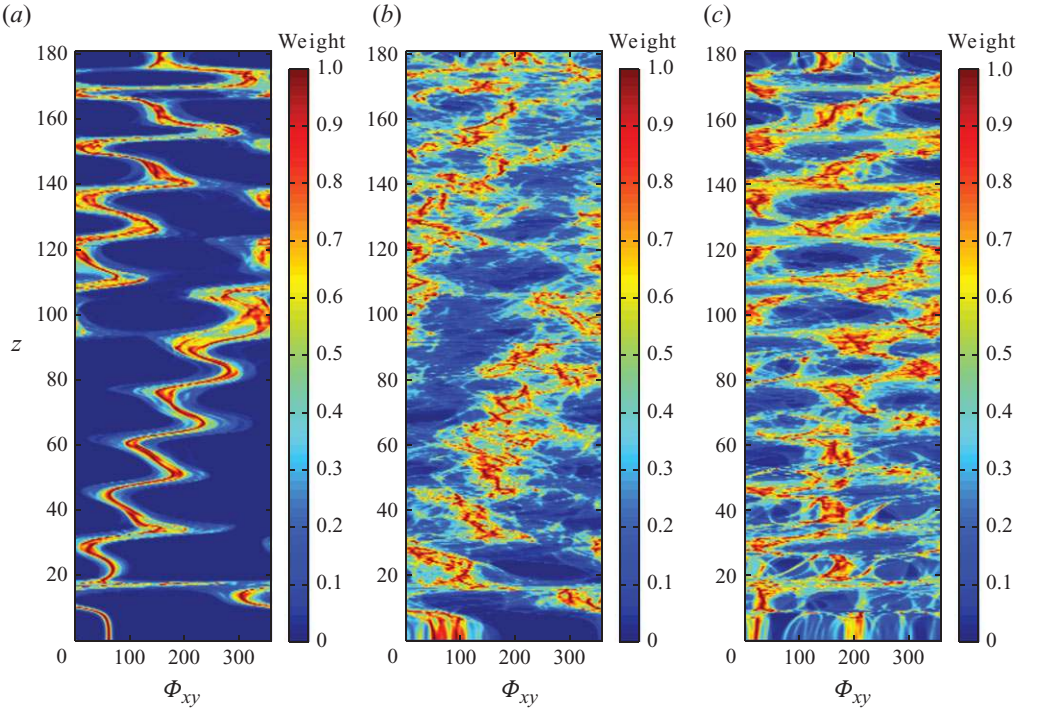

FIGURE 12. Histogram of the phase difference (3.5) along the cylinder span at (*a*) $Re_m = 110$, (*b*) $Re_m = 330$ and (*c*) $Re_m = 1100$.

cross-flow displacement nodes. In each cell the phase difference decreases by approximately $-80°$. As a result, a drift of the pattern towards higher phase angles occurs along the span (increasing z). It is interesting to note that this pattern is mainly located in the range $\Phi_{xy} \in [0°, 180°]$ in the high-velocity region, which means that counter-clockwise orbits are preferred in this region; this coincides with the experimental observations of Modarres-Sadeghi *et al.* (2010). The zigzagging pattern is altered beyond $z = 140$, where travelling waves are less pronounced.

A very similar analysis can be carried out at $Re_m = 330$. Even though noisier, the same pattern can be identified as counter-clockwise trajectories seem also predominant in the high-velocity region, except very close to $z = 0$. The case $Re_m = 1100$ exhibits some differences, as two peaks emerge near $z = 0$, which correspond to two possible synchronized states. The fact that a peak appears at $\Phi_{xy} \approx 30°$ around $z = 14$, whereas a peak exists at $\Phi_{xy} \approx 20°$ near $z = 5$, could appear to contradict the above-described clockwise/counter-clockwise alternating pattern in regions dominated by standing waves. In fact, a careful monitoring of the Φ_{xy} temporal evolution shows that this last peak is related to secondary peaks at $\Phi_{xy} \approx 215°$ ($z = 14$) and $\Phi_{xy} \approx 345°$ ($z = 14$), while $\Phi_{xy} \approx 30°$ ($z = 14$) and $\Phi_{xy} \approx 210°$ ($z = 5$) occur simultaneously. Therefore, the clockwise/counter-clockwise alternating pattern is preserved in this region as well. The standing character of the structural displacements is more pronounced at $Re_m = 1100$, which causes a distortion of the zigzagging pattern. In particular, larger jumps are observed between spanwise cells. In the high-velocity region ($10 < z < 60$), most of phase difference peaks occur between $0°$ and $180°$ with a preferential angle of

$\Phi_{xy} \approx 160°$. The drift towards higher angles along the span is less pronounced than in previous cases and occurs mainly beyond $z = 60$.

In all studied cases, synchronization states between in-line and cross-flow motions can be found along the cylinder span. A region of alternating clockwise/counter-clockwise motions can be identified near $z = 0$, where the standing character of the structure response dominates. Beyond this region, the distribution of phase difference between in-line and cross-flow vibrations follows a zigzagging pattern which occurs within the range $\Phi_{xy} \in [0°, 180°]$ in the high-velocity region, and is thus related to counter-clockwise orbits.

Next we proceed to correlate the observations made on the nature of the structural response and the synchronization between in-line and cross-flow motions with flow patterns and fluid–structure interaction mechanisms.

4. Coupled fluid–structure system

This section focuses on the fluid–structure interaction mechanisms causing the vibrations analysed in § 3. The occurrence of the lock-in phenomenon is studied in § 4.1, and an analysis of the wake patterns is presented in § 4.2. Finally, fluid forces and fluid–structure energy transfer are studied in § 4.3.

4.1. *Lock-in within shear flow*

The phenomenon of lock-in in flexibly mounted rigid cylinders within uniform flow consists of self-excited, VIV accompanied by the 'locking' of the frequency of vortex formation with the frequency of cylinder vibrations, rather than the Strouhal frequency, which is associated with the von Kármán instability behind a stationary cylinder. It has been investigated extensively in the literature, as reviewed by Bearman (1984) and Williamson & Govardhan (2004). This is an important feature of VIV; it has been shown, in particular, that maximum oscillation amplitudes occur under the lock-in condition. This synchronization can exist over a wide range of oncoming flow velocities, especially for low mass ratios.

Studies of rigid cylinders forced to vibrate harmonically at a prescribed amplitude and frequency have underscored the importance of the phenomenon of 'wake capture', i.e. the entrainment of the vortex shedding frequency relatively far from the Strouhal frequency (Sarpkaya 2004).

A long flexible cylinder in shear flow is also known to undergo self-induced vibrations, but the wake capture is exhibited only over part of the cylinder span; in the remaining part, the wake does not lock in to the structural vibration frequency. As a result, when a flexible structure undergoes VIV, we refer to a 'region of lock-in' versus a 'region of non-lock-in' across the span. Even within a lock-in region, the phenomenon of frequency entrainment is much more complex in shear flow because several frequencies may potentially be excited. Indeed, a uniform oncoming flow past a constant diameter cylinder induces a narrow excitation bandwidth, resulting in a single frequency of vortex shedding. In contrast, it is unclear for a non-uniform current how the flow–structure interaction mechanisms apply when several natural frequencies are within the bandwidth of excitation by the flow, and which frequency may dominate.

In the case of forced cross-flow oscillations of rigid and flexible cylinders in sheared currents, Stansby (1976) and Peltzer & Rooney (1985) have emphasized the formation of long ($>40D$) spanwise cells of constant shedding frequency equal to the forcing frequency. This partial lock-in of the wake perturbs the pattern observed in the case of

a stationary cylinder in shear flow (or stationary tapered cylinder in a uniform flow) that is composed of smaller cells separated by regular discontinuities of shedding frequency (Noack *et al.* 1991). For a long flexible cylinder constrained to oscillate in the cross-flow direction and using a low-resolution simulation, Lucor *et al.* (2001) have reported a partial lock-in spanwise distribution with a synchronization region located in the high-velocity zone, and an unsynchronized state region elsewhere.

A detailed analysis of the lock-in phenomenon is presented here for the flexible cylinder under study. *The lock-in condition at any location along the cylinder span is established when the frequency of the wake velocity oscillations coincides with the frequency of the local cross-flow structural response*; otherwise, we characterize the condition as non-lock-in. We define a 'lock-in region' of the structure to be a continuous part of the span which contains all locally locked-in locations. We pay particular attention to both the lock-in and non-lock-in regions, especially for the cases of multi-frequency response. The influence of lock-in/non-lock-in conditions on the fluid–structure energy transfer is addressed in § 4.3.

The vortex shedding frequency is established from the cross-flow component of the flow velocity, v, which was recorded over the same time interval as the structural displacements, along a spanwise line located downstream of the cylinder at $(x, y) = (20, 0)$. The PSD of the v velocity component is plotted along the span for the three Re_m in figure 13. Selected frequencies, previously identified by spectral analysis of the structure response (§ 3.2), are indicated by dashed lines. Two main spanwise regions can be distinguished in all cases: a region of lock-in, where the vortex shedding frequency coincides with the structural cross-flow vibration frequency (or frequencies, in the case of multi-frequency response), can be identified in the high-velocity region, near $z = 0$. The rest of the span corresponds to a non-lock-in region, where vortex shedding and structural vibrations are not synchronized.

The detailed plots of the lock-in regions are presented in figures 13(b), 13(d), 13(f). At $Re_m = 110$, lock-in occurs over $59D$, starting from $z = 0$. The case $Re_m = 330$ exhibits lock-in at the three distinct frequencies identified in the multi-frequency structural response. The region where vortex shedding is synchronized with at least one of these frequencies covers $75D$.

At $Re_m = 1100$, the spanwise evolution of the predominant frequency of v presents more irregular events than in previous cases due to the absence of stable wake patterns in several spanwise regions, as discussed in the following. These zones, where no predominant frequency peak can be identified, create 'holes' in the lock-in spanwise pattern. The synchronization zone can be referred to as a 'discontinuous lock-in region' and covers $77D$.

Two possible causes can be suggested to explain the tendency observed concerning the length increase of the lock-in region as Re_m increases, especially between $Re_m = 110$ and the two other cases. Previous studies on forced oscillations in shear flow (Stansby 1976; Peltzer & Rooney 1985) have reported that the lock-in region grows in size as the oscillation amplitude increases. Such an increase in the oscillation amplitude is observed in the present case as a function of Re_m (figure 4). Another possible explanation is related to a larger variation of the Strouhal number in the region $z \in [50, 80]$ in the case $Re_m = 110$ ($Re \in [75, 90]$) than at higher Re_m (Williamson 1992; Braza, Faghani & Persillon 2001).

It can be noted that for $z \in [0, 80]$ approximately, the quasi-static bending of the cylinder, due to the time mean component of drag force, can tend to oppose the shear flow effect by increasing the magnitude of the velocity component normal to the cylinder for increasing z. For $z > 80$, approximately, the structural static bending can

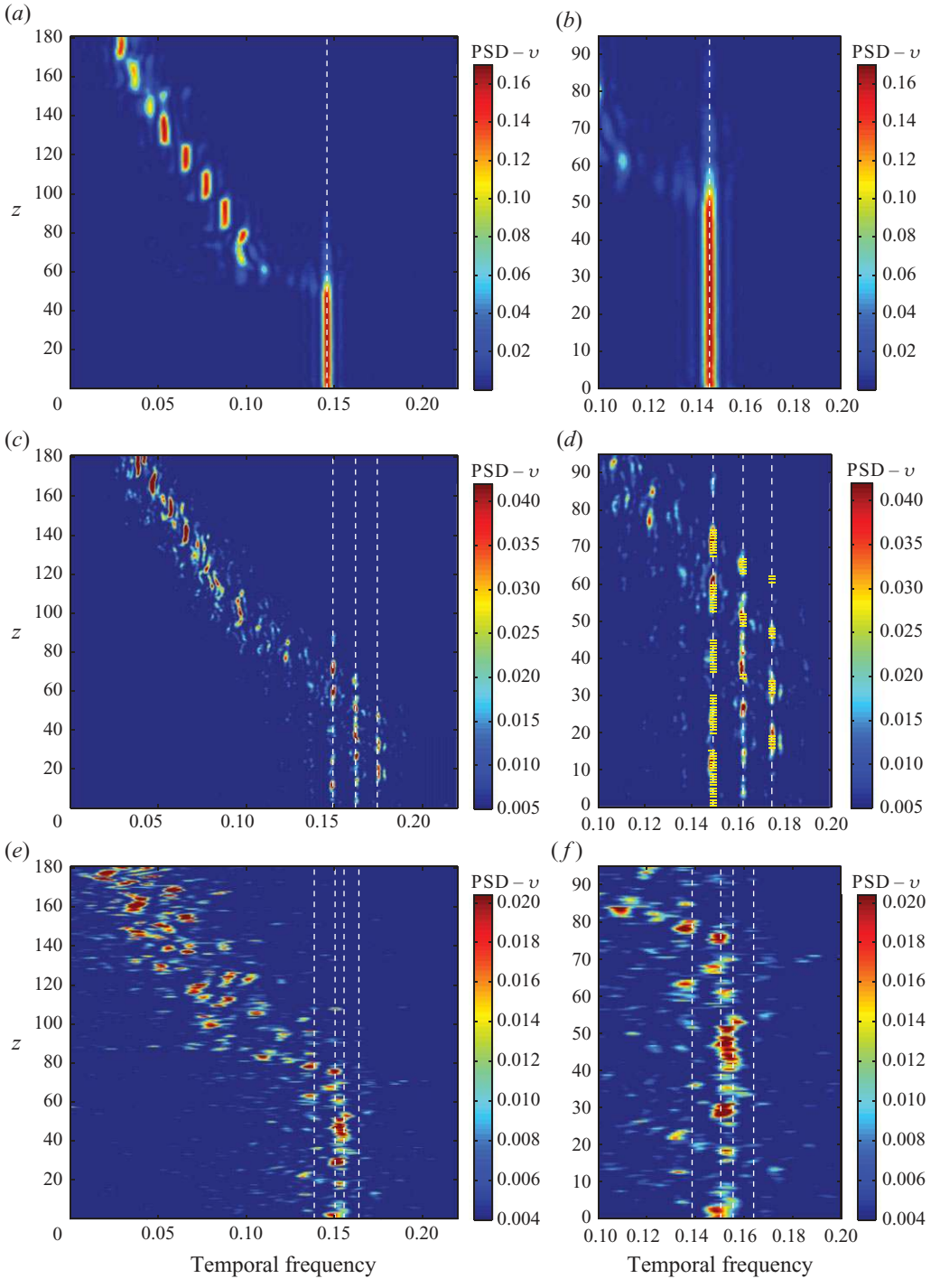

FIGURE 13. PSD of the temporal evolution of the cross-flow component of the flow velocity along a spanwise line at $(x, y) = (20, 0)$, at (a,b) $Re_m = 110$, (c,d) $Re_m = 330$ and (e,f) $Re_m = 1100$. The detailed views of lock-in regions are plotted in (b,d,f). The white dashed lines indicate the frequencies identified in figure 6. In (d), the yellow dashes indicate the local predominant structure vibration frequency identified from figure 6(c).

increase the effect of the shear flow by reducing the flow normal velocity component, as z increases.

Under the lock-in condition, large deviations from the Strouhal shedding frequency are observed. The non-dimensional local shedding frequency is defined as $f_l = f/U_l$, where f is the local predominant frequency non-dimensionalized by U, the maximum oncoming flow velocity ($z = 0$), and U_l is the local oncoming flow velocity non-dimensionalized by U. The local shedding frequencies identified at lock-in are in the ranges $f_l \in [0.146, 0.191]$, $f_l \in [0.149, 0.221]$ and $f_l \in [0.151, 0.216]$ for $Re_m = 110$, $Re_m = 330$ and $Re_m = 1100$ respectively.

In the case of multi-frequency response ($Re_m = 330$), the spectral analysis carried out in § 3.2 revealed that three frequencies can contribute to the structural cross-flow vibration at a given spanwise location. In this context, the question arises whether the vortex shedding is synchronized with preferentially a single frequency. Despite some secondary peak contributions, figure 13(d) shows that, at each spanwise location, the vortex shedding is mainly synchronized with a single frequency, which can be a different one for each location. It has been emphasized previously that multi-frequency responses are instantaneously mono-frequency and that the globally multi-frequency character is due to a temporal evolution of the excited frequency. Hence, at a given spanwise location vortex shedding occurs mainly at a single frequency, while the structural vibration frequency may vary among the predominant vibration frequencies. As a consequence, the lock-in condition does not occur continuously as a function of time.

These observations raise a second question regarding which vibration frequency is selected by the wake to lock-in. In figure 13(d), yellow dashes are used to indicate the local predominant structure vibration frequency issued from figure 6(c). The discontinuous line formed by these yellow dashes describes the lock-in pattern relatively accurately, showing that the wake lock-in frequency corresponds to the local predominant vibration frequency. It should be noted that some exceptions exist as for $z \in [24, 28]$ where lock-in occurs at a vibration frequency equal to 0.162, while this frequency has a secondary but significant contribution to the structural vibration in this region.

In non-lock-in regions, a global decrease of the vortex shedding frequency is observed along the span, in agreement with the spanwise decrease of the local shedding frequency based on the Strouhal number, the local Strouhal frequency, which follows the linear reduction of the oncoming flow velocity. In the cases $Re_m = 110$ and $Re_m = 330$, a cellular pattern can be clearly identified: spanwise regions of constant shedding frequencies are separated by discontinuities. The frequency within a cell remains constant along its length; hence, the locations away from the centre of the cell violate the local Strouhal frequency; at the ends of the cell a threshold event is reached, and a new cell starts accompanied by a discontinuous jump in frequency to better agree with the local Strouhal frequency.

The question arises: what is the event that triggers the end of a cell? Similar cellular patterns have been reported for stationary cylinders in shear flow and tapered cylinders in uniform flow (e.g. Gaster 1971; Griffin 1985; Peltzer & Rooney 1985; Noack *et al.* 1991; Piccirillo & Van Atta 1993). These previous works have emphasized the influence of several parameters on the cell length, such as for instance the shear parameter, the cylinder aspect ratio and the Reynolds number. For a stationary cylinder of aspect ratio $L/D = 107$ and a comparable shear parameter, Peltzer & Rooney (1985) observed spanwise cells of 11 diameters on average, at a higher Reynolds number. Here, the cases $Re_m = 110$ and $Re_m = 330$ exhibit cells of $13D$–$16D$

which correspond approximately to half of the excited wavelength in the cross-flow direction. At $Re_m = 110$, it can be noticed that frequency discontinuities between cells coincide roughly with the nodes of the structural response. Moreover, it can be observed that the cellular pattern exists beyond $z \approx 140$ (Re <48), while vortex shedding vanishes in this region as shown in the following. This is due to a persisting undulation of the wake, probably triggered by the adjacent vortex shedding. Similar observations can be made concerning the forcing of the cellular pattern by structural vibration in the case $Re_m = 330$. However, the existence of three competing excited wavenumbers induces less sharp transitions between cells, since vibration nodes are moving in the spanwise direction. At $Re_m = 1100$, the non-lock-in region exhibits a noisier frequency distribution, illustrating the increased complexity of the wake patterns; however, the general tendency towards decreasing shedding frequency along the span as well as the appearance of frequency discontinuities are clearly visible. In summary, the half-wavelength of the local cross-flow structural vibrations seems to be a significant parameter for the formation of cells.

A comparison of the lock-in/non-lock-in spanwise distribution and in-line/cross-flow motion synchronization patterns (figure 12) shows that counter-clockwise orbits are the most likely trajectories under the lock-in condition. This corroborates the experimental observations of Dahl *et al.* (2007) who reported that, for a rigid cylinder in uniform flow, regular 'figure-eight' motions as those described in the present study are generally associated with counter-clockwise orbits at lock-in. This point is discussed from the fluid–structure energy transfer point of view in § 4.3.

To summarize, the lock-in region is located in the high-velocity zone and represents approximately 30 %, or more, of the total cylinder length. In this region, spatial intermittencies of lock-in can be observed. In the case of multi-frequency response, the wake is mainly synchronized with a single frequency in each particular location along the cylinder, that is mainly the locally predominant vibration frequency. The non-lock-in region is characterized by a cellular pattern as in the case of a stationary cylinder in shear flow.

4.2. *Wake patterns*

In this section, the wake patterns behind the cylinder are studied in light of the lock-in/non-lock-in spanwise distribution identified in § 4.1. The objective is to clarify the interaction between wake structures and cylinder motions that leads in shear cross-flows to the formation of a mixed standing and travelling wave response.

For better visualization of the wake patterns, instantaneous iso-surfaces of spanwise vorticity (ω_z) are presented in figure 14. Only part of the computational domain is plotted downstream of the cylinder: $[0.6D, 32D]$, $[0.6D, 25D]$ and $[0.6D, 20D]$ for the cases $Re_m = 110$, $Re_m = 330$ and $Re_m = 1100$, respectively. The effect of the transition to turbulence as Re_m increases is visible in these plots.

For $Re_m = 110$, the Reynolds number is in the range $[30, 110]$. The strongly three-dimensional wake observed here, which is different than the wake behind a straight rigid cylinder in uniform flow, is due to the joint effects of shear flow, cylinder static bending due to the time mean component of the drag force and cylinder vibrations. For $Re_m = 330$, the Reynolds numbers are within the range where the secondary instability, corresponding to a spanwise undulation of the von Kármán vortices, develops in the wake of a straight stationary cylinder in uniform flow. Different transition patterns have been reported in this context and are related to the characteristic wavelengths of the secondary instability. The A- and B-mode transition patterns have been studied both experimentally (e.g. Williamson & Roshko 1988;

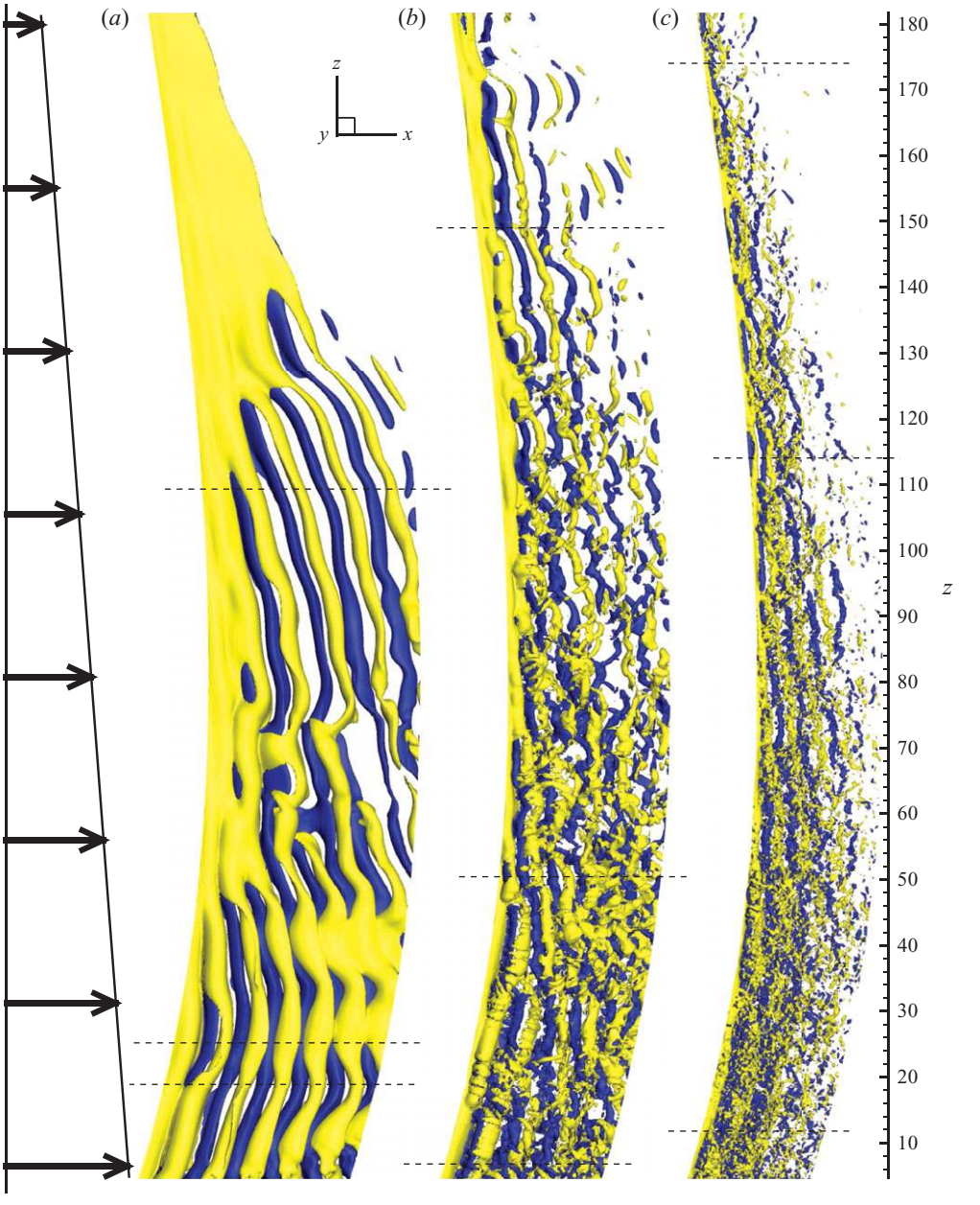

FIGURE 14. Instantaneous iso-surfaces of spanwise vorticity (ω_z) downstream of the cylinder at (*a*) $Re_m = 110$, $\omega_z = \pm 0.13$, (*b*) $Re_m = 330$, $\omega_z = \pm 0.3$, and (*c*) $Re_m = 1100$, $\omega_z = \pm 0.8$. The arrows represent the linear shear oncoming flow. The dashed lines indicate the locations of the (x, y) planes presented in figure 18.

Williamson 1992) and numerically (e.g. Braza *et al.* 2001). Another transition pattern, the C-mode, has also been put forward in particular in the case of forced asymmetry (Zhang *et al.* 1995). In the present case, the secondary instability is affected by the previously mentioned sources of three-dimensionality, as illustrated in figure 14(*b*).

The case $Re_m = 1100$ exhibits a more developed turbulent wake, but the von Kármán vortices are still visible.

At lock-in, vortex shedding occurs at the same frequency (or frequencies, in the case of multi-frequency vibrations) over a long spanwise region ($>59D$), while the oncoming flow velocity varies linearly. This results in an oblique vortex shedding pattern where the distance between two consecutive vortex rows decreases along the span, due to the difference in the convective velocity, for increasing z. Such an oblique vortex shedding pattern has been reported in the literature in uniform flows perturbed by end effects (Williamson 1989), as well as in shear flows past stationary cylinders (Mukhopadhyay, Venugopal & Vanka 1999), and uniform flows past tapered cylinders (Gaster 1971; Piccirillo & Van Atta 1993). The oblique shedding pattern is clearly visible in the lock-in region for example for $z \in [20, 55]$ at $Re_m = 110$. This orientation of the vortex shedding is illustrated by further detailed flow visualizations in the following.

In the case of forced standing wave motions in uniform flow, Newman & Karniadakis (1997) have reported an interwoven wake structure due to alternating positive and negative cross-flow displacements and the 180° phase difference between two adjacent anti-nodes. In particular, the connections between co-rotating vortex rows present a spanwise symmetry about the anti-nodes. This pattern is strongly modulated in the present case of free vibrations in shear flow. Connections between vortex rows are not symmetrical and are oriented according to the above-mentioned oblique shedding pattern. The alternating near-nodes and anti-nodes of cross-flow vibration induce, however, a spanwise undulation of the vortex rows.

As shown in §4.1, the identifiable wake patterns in the non-lock-in region ($Re_m = 110$, $Re_m = 330$) consist of spanwise cells of constant shedding frequency each, similar to the case of a stationary tapered cylinder in uniform flow or a stationary cylinder in shear flow, as described, for example, in Gaster (1971), Piccirillo & Van Atta (1993) and Mukhopadhyay *et al.* (1999). There are two principal features: oblique vortex shedding in each cell and vortex splittings between adjacent cells. As reported above, oblique vortex shedding also occurs within the lock-in region. No vortex shedding is found beyond $z \approx 140$ ($Re < 48$) at $Re_m = 110$.

The observed vortex splitting is required to ensure continuity of the spanwise vorticity filaments, since the shedding frequency is discontinuous as we cross from one cell to the next. Vortex splitting is referred to as 'vortex dislocation' in studies of stationary cylinders in uniform flow (Williamson 1992), and also as 'vortex adhesion points' (Zhang *et al.* 1995). Similar vortex splitting has been observed in studies of shear flows past uniform cylinders or uniform flows past stationary and moving tapered cylinders (e.g. Piccirillo & Van Atta 1993; Techet *et al.* 1998; Mukhopadhyay *et al.* 1999).

When lock-in occurs at more than one frequency, as in the case $Re_m = 330$, vortex splitting is also observed within the lock-in region. Several vortex splitting events can be observed in figure 14, while detailed visualizations of this phenomenon are provided in the following.

In figure 15, the instantaneous iso-surfaces of spanwise vorticity are plotted in selected regions of the wake and at different instants in time. Figure 15(a) focuses on the lock-in/non-lock-in transition region where nine vortex rows (lock-in region) are connected to six vortex rows (non-lock-in region) via multiple vortex splittings. Figures 15(b) and 15(c) illustrate the oblique vortex shedding pattern in the non-lock-in region, as well as vortex splittings. Even in the very near region, the wake exhibits strong oblique shedding. As can be observed in figure 15(c), vortex splittings can occur simultaneously between several adjacent cells.

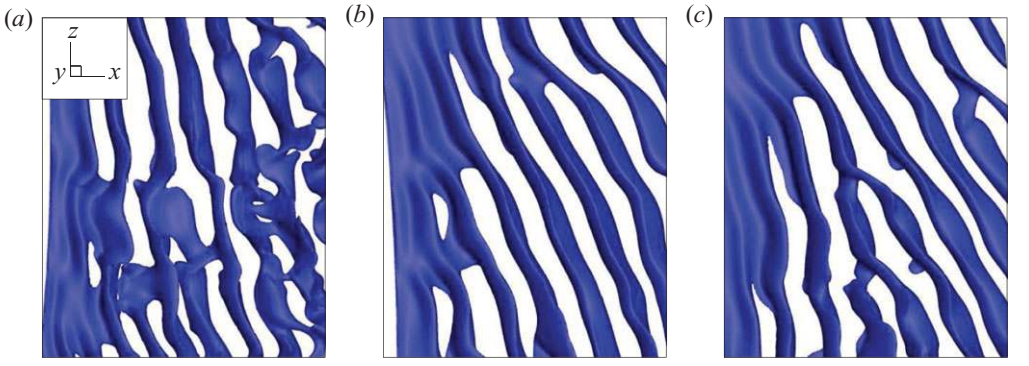

FIGURE 15. (Colour online available at journals.cambridge.org/FLM) Instantaneous iso-surfaces of spanwise vorticity (ω_z) downstream of the cylinder in the case $Re_m = 110$, $\omega_z = -0.045$: (*a*) $z \in [47, 100]$, (*b*) $z \in [84, 134]$ and (*c*) $z \in [86, 136]$. Several snapshots at different instants are presented.

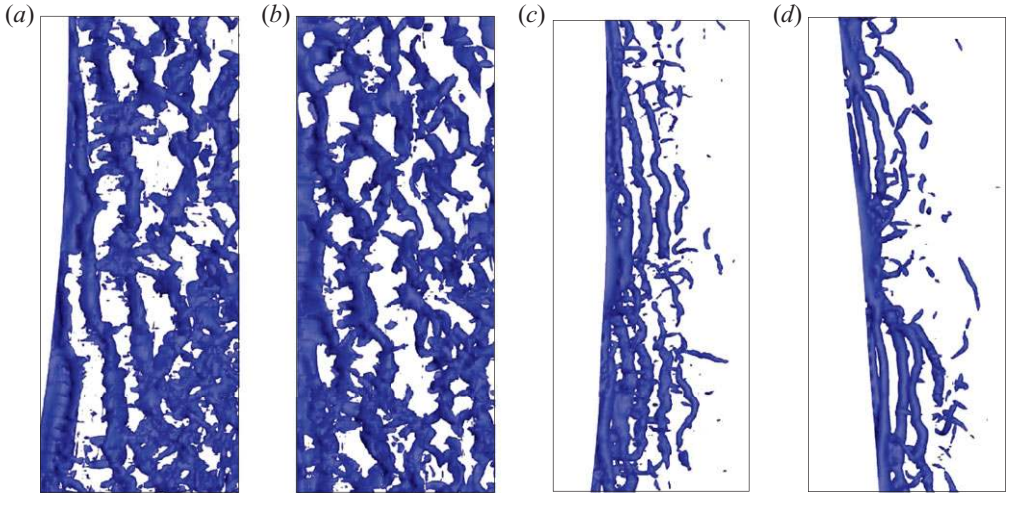

FIGURE 16. (Colour online) Instantaneous iso-surfaces of (*a*, *b*) spanwise vorticity (ω_z) in the case $Re_m = 330$ and (*c*, *d*) pressure in the case $Re_m = 1100$, downstream of the cylinder: (*a*) $z \in [32, 80]$, $\omega_z = -0.24$, (*b*) $z \in [75, 128]$, $\omega_z = -0.14$, (*c*) $z \in [49, 92]$, $p = -0.13$, and (*d*) $z \in [107, 141]$, $p = -0.09$. Several snapshots at different instants are presented.

A detailed visualization of the wake patterns at $Re_m = 330$ and $Re_m = 1100$ is presented in figure 16. The oblique vortex shedding pattern is illustrated in figures 16(*a*) and 16(*c*), which show iso-surfaces of spanwise vorticity and negative pressure. As noted previously, the oblique orientation of the vortices relative to the cylinder axis can be identified in the near region, closest to the cylinder. The orientation of the vortex rows, observed in all cases studied herein, can be related to the orientation of the travelling wave component of structural vibrations described in § 3.2. The oblique peeling-off of the vortices as they form, i.e. the travelling vortex shedding phase, appears to 'drive' the travelling wave component from high- to low-velocity regions.

At $Re_m = 330$ the spanwise discontinuities of the lock-in frequency lead to multiple vortex splittings in the lock-in region (figure 16*a*). Vortex splittings are also observed

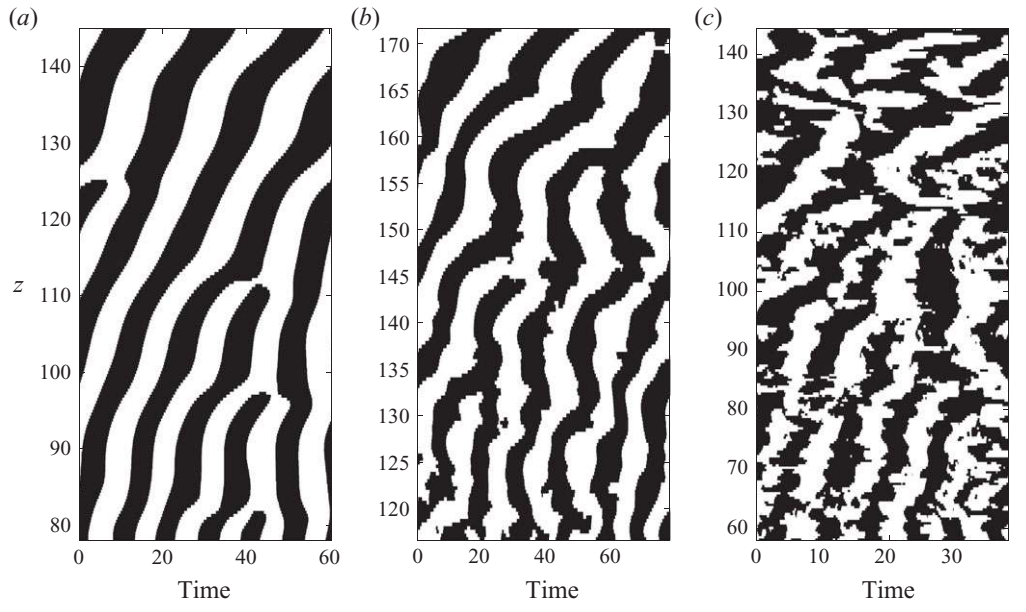

FIGURE 17. Selected time series of the cross-flow component of the flow velocity along selected spanwise regions at $(x, y) = (20, 0)$, at (a) $Re_m = 110$, (b) $Re_m = 330$ and (c) $Re_m = 1100$. Positive (negative) values are plotted in white (black).

in the non-lock-in region as shown in figure 16(b). The triangle-shaped connections appearing between some rows of vortices near cross-flow vibration nodes resemble those reported by Newman & Karniadakis (1997) in uniform flow. The structural motion has a strong influence on the wake in the non-lock-in region as illustrated in figure 16(d) at $Re_m = 1100$: in certain zones, no well-defined vortex rows can be identified in the vicinity of vibrational nodes, while the vortices shed in adjacent cells are bent and seem to merge together in nodal regions.

Figure 17 depicts the spatio-temporal evolution of the cross-flow component of the flow velocity downstream of the cylinder, at several time intervals. Vortex splittings are associated with spanwise bifurcations in the cross-flow velocity patterns. These events can be isolated in time and space, but also often occur in groups or in cascade. No periodicity in vortex splitting has been identified in the present study.

Several investigations have been carried out to identify and classify the vortex shedding patterns occurring in the wake of vibrating rigid cylinders in uniform flow (Williamson & Roshko 1988; Jeon & Gharib 2001; Jauvtis & Williamson 2004; Carberry, Sheridan & Rockwell 2005). When there are spanwise variations in the configuration, Techet *et al.* (1998) and Flemming & Williamson (2005) have shown the possible co-existence of different shedding patterns along the span. In the case of flexible cylinders, the experimental studies of Brika & Laneville (1993) and more recently Huera-Huarte & Bearman (2009*b*) have shown that two principal 'vortex modes', characterized by two single vortices per cycle (2S mode) and two pairs of vortices per cycle (2P mode), dominate the wake.

As previously detailed, the wake of the present freely vibrating cylinder mainly consists of oblique vortex rows, often inter-connected through vortex splittings. It is important to note that almost periodic shedding patterns can be identified only in some spanwise regions. In addition, strong modulations due to the combined effects

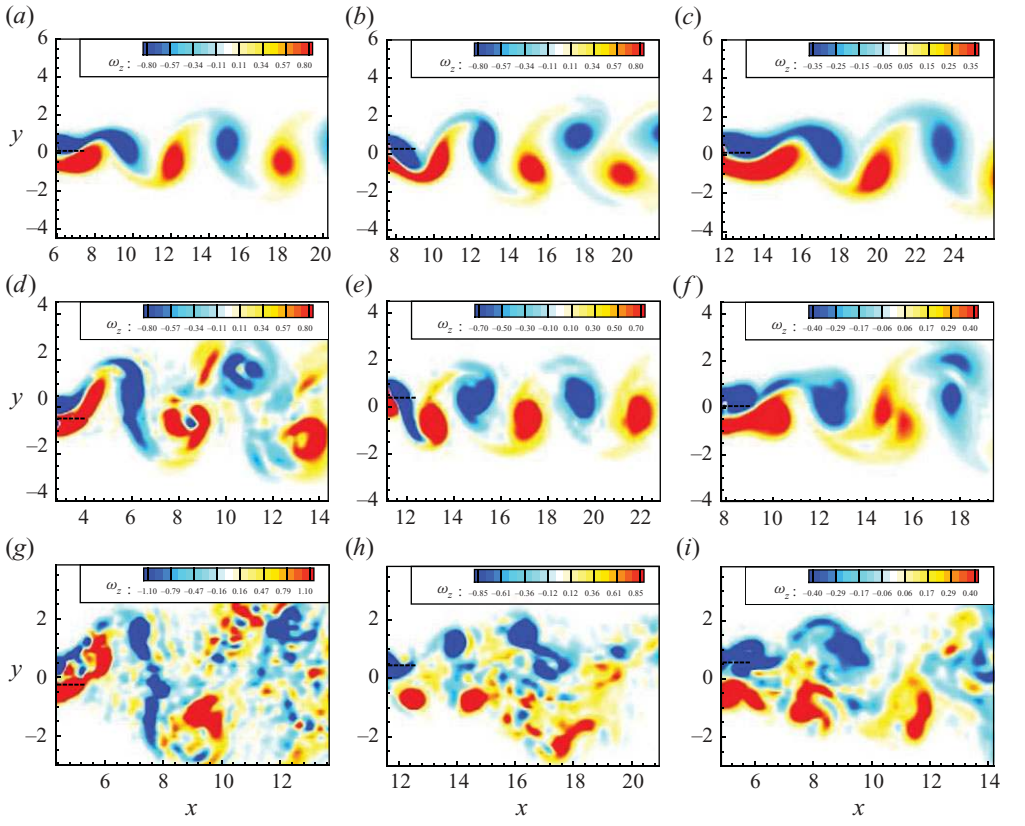

FIGURE 18. Instantaneous iso-contours of spanwise vorticity in the (x, y) plane, in the near wake, at $(a–c)$ $Re_m = 110$, $(d–f)$ $Re_m = 330$, $(g–i)$ $Re_m = 1100$. The spanwise locations of the (x, y) planes are indicated in figure 14 by dashed lines: (a) $z = 18$, (b) $z = 25$, (c) $z = 109$, (d) $z = 7$, (e) $z = 50$, (f) $z = 149$, (g) $z = 12$, (h) $z = 114$ and (i) $z = 174$. The cylinder centre position is indicated by short dashed segments. Several snapshots at different instants are presented.

of shear flow, multiple vortex splittings, structural bending and structural vibrations, limit a clear definition of these patterns to an area close to the cylinder, the near-wake zone, especially at $Re_m = 330$ and $Re_m = 1100$. In these cases, a major part of the near wake is dominated by irregular and intermittent patterns, that cannot always be classified according to the canonical patterns identified by Williamson & Roshko (1988) for a rigid cylinder in uniform flow.

In some cases, however, wake patterns resembling the canonical shedding modes can be identified, as illustrated in figure 18, where the instantaneous iso-contours of the spanwise vorticity are plotted in selected (x, y) planes, downstream of the cylinder. The spanwise locations of the corresponding (x, y) planes are indicated by dashed lines in figure 14. The cylinder position is indicated by short dashed segments in figure 18. At $Re_m = 110$, a shedding pattern resembling a 2S mode is observed on most of the cylinder span, including the non-lock-in region (figures 18*a*, 18*b* and 18*c*). At lock-in, the vibration amplitude has an influence on the wake width as illustrated in figures 18(a) and 18(b), which correspond to the planes located near a node and an anti-node of the structural cross-flow motion, respectively. The absence of 2P shedding patterns at this Reynolds number is in agreement with the study of Williamson &

Govardhan (2004). In the cases $Re_m = 330$ and $Re_m = 1100$, a pattern resembling a 2P mode can be identified intermittently in the high-velocity zone, within the lock-in region, as shown in figures 18(*d*) and 18(*g*). This shedding mode is not observed in the non-lock-in region. When identifiable, vortex patterns are mostly dominated by 2S-like modes in both the lock-in and non-lock-in regions (figures 18*e*, 18*h* and 18*i*). A shedding pattern resembling a 2C mode, characterized by two co-rotating vortices per half-cycle (Flemming & Williamson 2005), can develop in the wake in the non-lock-in region (figure 18*f*).

The mutual influence of the wake patterns and the cylinder vibrations is evident, in particular through the lock-in phenomenon, and the strong link between oblique vortex shedding and the orientation of the travelling wave component of the structural response. A detailed quantification of fluid forces and fluid–structure energy transfer mechanisms is provided in the next section.

4.3. *Fluid forces and fluid–structure energy transfer*

In this section we study the fluid forces exerted on the cylinder and relate them to the cylinder vibrations and wake patterns analysed in §§ 3 and 4.2. These forces are representative of nonlinear equilibrium states reached by the coupled fluid–structure system and can be used to identify the spatio-temporal properties of the fluid–structure energy transfer. Such energy exchanges are critical to the phenomenon of VIV and have both theoretical interest and impact on applications.

The evolution of the drag and lift coefficients in space and time, which correspond to the results of the cylinder vibrations presented in figures 2 and 3, are plotted in figures 19 and 20. The fluid forces include both the pressure and viscous components and are normalized by the local oncoming flow velocity; they are denoted by C_d and C_l, to avoid confusion with C_x and C_y, which are normalized using the maximum velocity. The evolution of the force coefficients is strongly affected by the cross-flow vibrations; the maxima of the drag coefficient are located in the region of the anti-nodes of cross-flow motion. This is in agreement with the experimental observations of Huera-Huarte, Bearman & Chaplin (2006) obtained from a flexible cylinder within a stepped current. Both standing and travelling aspects of structural motion are clearly visible, while, as previously mentioned, it can be noticed that the standing wave pattern is more pronounced in the case $Re_m = 1100$.

Occasional non-stationary behaviour can be observed in the evolution of both coefficients, especially for $Re_m = 330$. This behaviour is exhibited simultaneously in the structural vibrations (figures 2*b* and 3*b*). The lowest values of the amplitude of the lift coefficient occur in the lock-in region. In the non-lock-in region, the lift force amplitudes increase relatively regularly along the span, while the drag coefficient exhibits a similar behaviour in the non-lock-in region, as confirmed by the maximum and r.m.s. values shown in figure 21. It can be noticed that both coefficients reach very high magnitudes in the non-lock-in region, compared to the case of a stationary cylinder, reported for example in Persillon & Braza (1998). Despite the influence from Re_m on the force coefficient amplitudes, the three Reynolds number cases present comparable spanwise trends. The very high amplitudes of the lift and drag coefficients in the non-lock-in region are due to the non-dimensionalization based on the local current velocity that linearly decreases along the span, while the structural motions lead to significant fluid forces; this representation, however, adds insight into how local forces relate to the local velocity in a sheared current.

The force coefficient in phase with the cylinder velocity is used to quantify the fluid–structure energy transfer in a similar way as used in Newman & Karniadakis

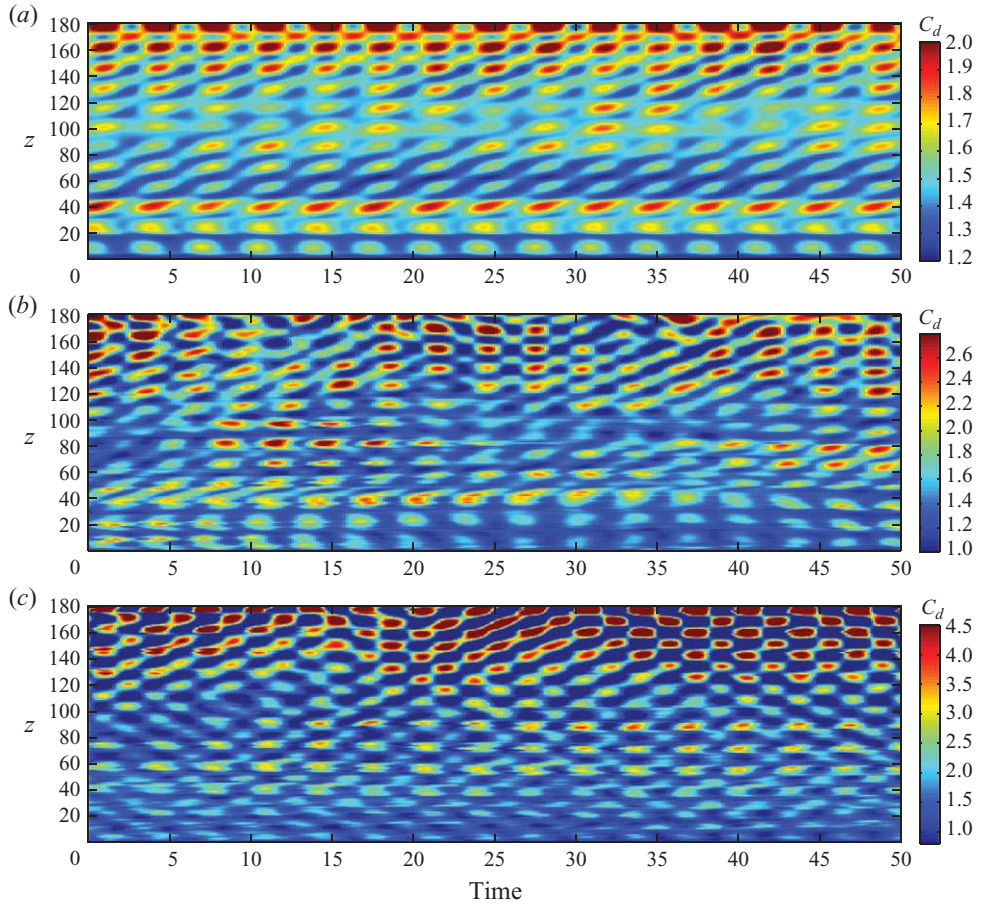

FIGURE 19. Temporal evolution of drag coefficient along the cylinder span at (*a*) $Re_m = 110$, (*b*) $Re_m = 330$ and (*c*) $Re_m = 1100$.

(1997), Hover, Techet & Triantafyllou (1998) and Dahl *et al.* (2010). The present analysis includes both in-line and cross-flow contributions of this coefficient. The time-averaged force coefficient in phase with the cylinder velocity is defined as

$$C_{fv}(z) = \frac{\dfrac{2}{T_s}\displaystyle\int_{T_s} (\tilde{C}_x(z,t)\dot{\tilde{\xi}}_x(z,t) + C_y(z,t)\dot{\xi}_y(z,t))\,\mathrm{d}t}{\sqrt{\dfrac{2}{T_s}\displaystyle\int_{T_s} \left(\dot{\tilde{\xi}}_x^2(z,t) + \dot{\xi}_y^2(z,t)\right)\mathrm{d}t}}, \tag{4.1}$$

where $\tilde{C}_x$ is the fluctuating component of the drag coefficient and $\dot{p}$ denotes the time derivative of p. The lift and fluctuating drag coefficients are based on the maximum oncoming flow velocity U ($z = 0$) so that C_{fv} is representative of the relative contribution of each spanwise location to the overall energy transfer. C_{fv} quantifies the power developed by the fluid acting on the vibrating cylinder. Positive C_{fv} implies that the fluid supplies, on average, energy to the structure and hence excites cylinder vibration, while negative C_{fv} indicates that the fluid is damping the cylinder motion.

The spanwise distribution of C_{fv} is plotted in figures 22(*a*), 22(*c*) and 22(*e*) for the three Re_m studied. Regions of positive C_{fv} are located in the high-velocity zone for all

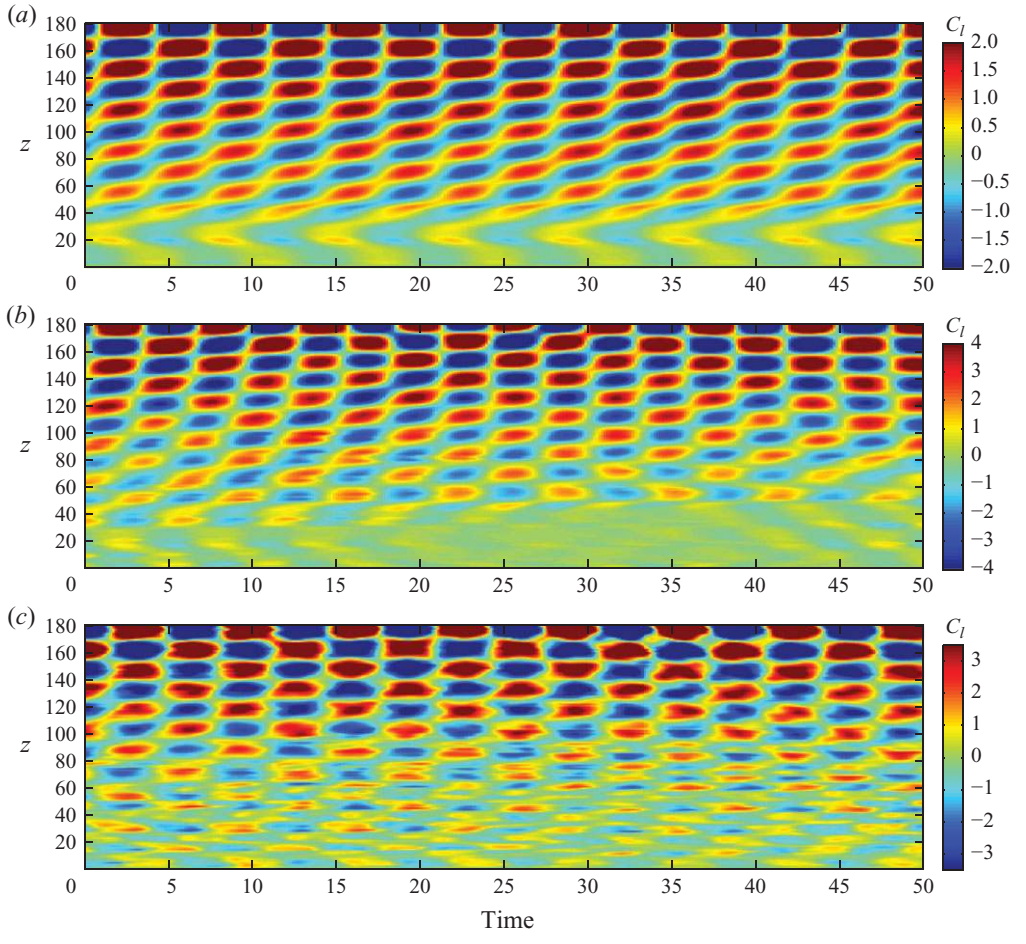

FIGURE 20. Temporal evolution of lift coefficient along the cylinder span at (*a*) $Re_m = 110$, (*b*) $Re_m = 330$ and (*c*) $Re_m = 1100$.

Re cases, corresponding principally to the lock-in regions. In the non-lock-in region, C_{fv} remains negative. To study the relation between lock-in/non-lock-in conditions and fluid–structure energy transfer, a frequency decomposition of C_{fv} is presented in figures 22(*b*), (*d*) and (*f*). Previously selected vibration frequencies (§ 3.2) are indicated by dashed lines. It can be observed that energy transfer occurs essentially at cross-flow vibration frequencies. The contributions of in-line vibration frequencies ([0.24, 0.36]) are negligible and are not presented here.

Positive energy transfer occurs under the lock-in condition, as a comparison of the lock-in pattern (figure 13) and the C_{fv} frequency decomposition (figure 22) shows. Negative values of C_{fv} can be observed within the lock-in region, especially near structural vibration nodes. It is recalled that we refer only loosely to 'nodes of structural vibration', because they are not strictly nodes in the sense of zero local motion, because of the superimposed travelling wave component. Spatial interruptions in the lock-in pattern can induce spanwise variations of C_{fv} as observed in the case $Re_m = 1100$.

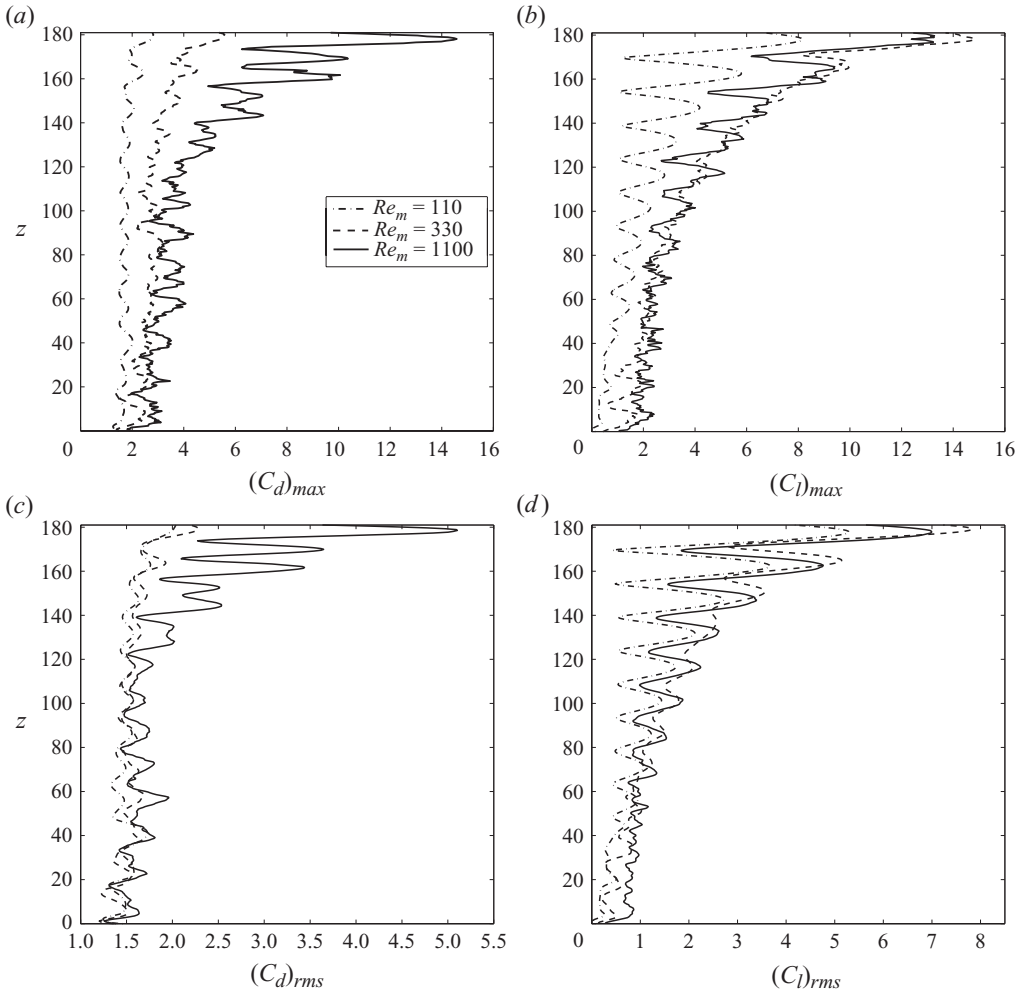

FIGURE 21. (a,b) Maximum and (c,d) r.m.s. values of (a,c) drag and (b,d) lift coefficients along the cylinder span.

In the case $Re_m = 330$, which exhibits a multi-frequency response, it has been shown previously that lock-in occurs mainly at a single frequency at each spanwise location; as a consequence, positive energy transfer at each location is expected to occur mainly at this frequency. This is verified in figure 22(d), where white dashes are used to indicate the local predominant lock-in frequency as determined from figure 13(d): the three main peaks of positive C_{fv} ($z \approx 18$, $z \approx 38$, $z \approx 57$) occur at the locally predominant lock-in frequencies.

Within the lock-in region, C_{fv} exhibits large spanwise variations. As noted, negative peaks can occur near vibration nodes in all studied cases. C_{fv} can also be influenced by in-line/cross-flow motion synchronization. Near $z = 0$, a standing wave-like synchronization pattern has been identified, with alternating counter-clockwise and clockwise trajectories as z increases (figure 12). The passage from counter-clockwise to clockwise motion can be related to a significant reduction of C_{fv}. For a rigid cylinder in uniform flow, Dahl *et al.* (2007) reported that counter-clockwise orbits are more favourable to stable vibrations. Such orbits

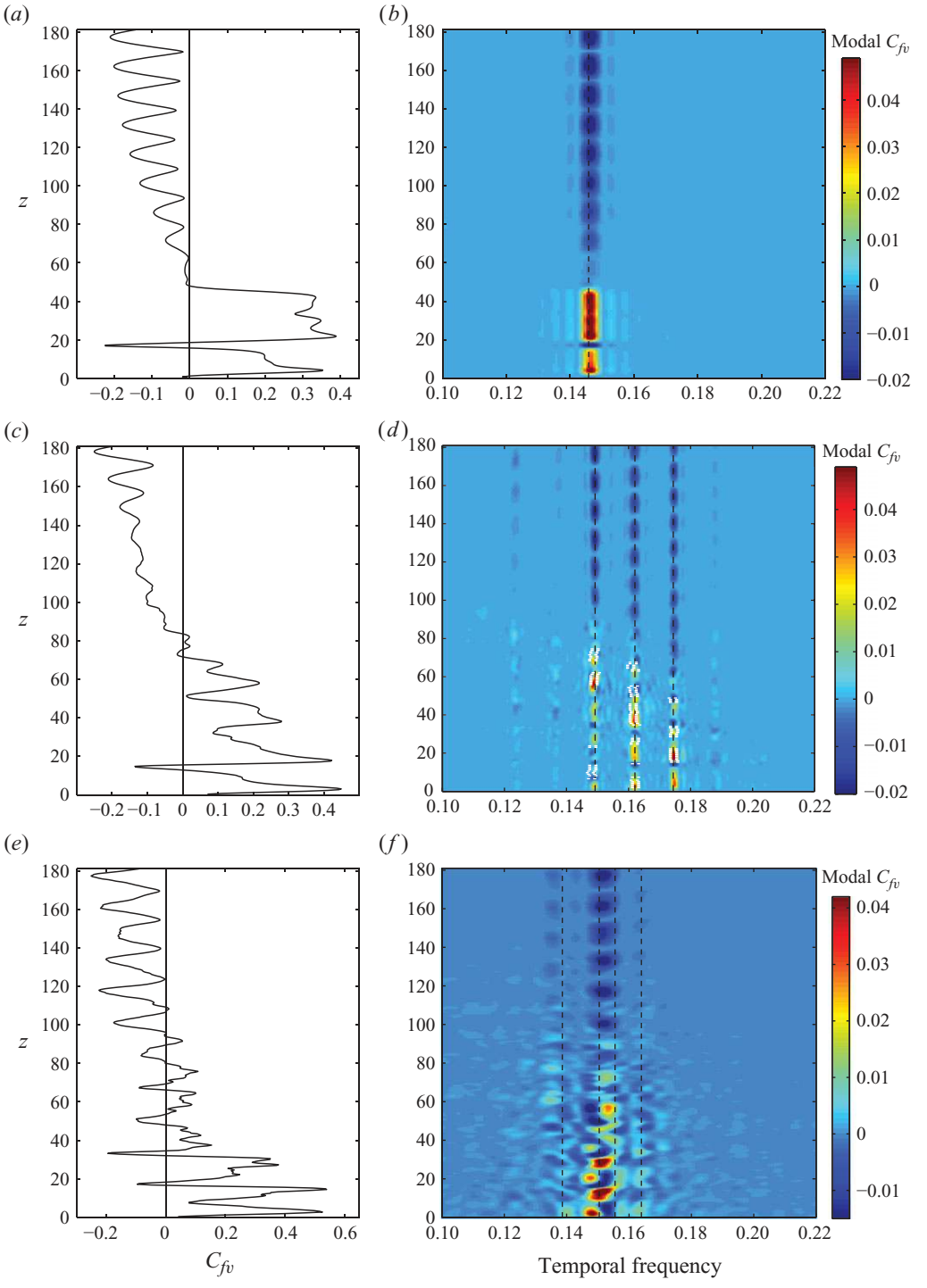

FIGURE 22. Force coefficient in phase with the cylinder velocity along the cylinder span: (a,c,e) total and (b,d,f) frequency decomposition, at (a,b) $Re_m = 110$, (c,d) $Re_m = 330$ and (e,f) $Re_m = 1100$. The black dashed lines indicate the frequencies identified in figure 6. In (d), the white dashes indicate the local predominant vortex shedding frequency obtained from figure 13 (d).

lead to larger vorticity generation at the extremes of cross-flow motion, while the cylinder moves downstream as it crosses the zero transverse position ($y = 0$), hence coming in close proximity to the recently shed vortices, resulting in high suction forces.

The predominant relative contribution of the third harmonic of lift observed for a rigid cylinder in uniform flow has been explained by the fact that, at very low structural damping, the first harmonic component of the lift coefficient has to be close to zero if the structure exhibits a regular, almost periodic figure-eight motion (Dahl *et al.* 2007, 2010). Pronounced third harmonic of the lift coefficient is not observed in the present case of a flexible cylinder in shear flow. Here, excitation zones in the high-velocity region are balanced by damping zones, mainly located in the non-lock-in region.

Within the non-lock-in region, C_{fv} exhibits a more regular spanwise pattern: negative peaks are observed near vibration anti-nodes and $C_{fv} \approx 0$ near vibration nodes.

The present analysis shows that the properties of the fluid–structure energy transfer mechanisms are determined by lock-in/non-lock-in conditions and are also influenced by in-line/cross-flow motion synchronization. The cylinder motion is driven by flow energy input within the lock-in region, located in the high-velocity region, where counter-clockwise trajectories dominate the in-line/cross-flow motion synchronization. The structural motion is damped by the flow within the non-lock-in region.

5. Conclusions

The vortex-induced vibrations of a long cylindrical tensioned beam in shear flow contain a mixture of standing and travelling waves in both the in-line and cross-flow directions. In all three Reynolds numbers studied, from 110 to 1100, the standing wave character appears predominantly near the ends, its contribution increasing with Reynolds number. Travelling waves, moving preferentially from high- to low-velocity regions, develop in the main part of the structure, between the two ends. The main features of the structural response and of the fluid–structure interaction mechanisms remain the same in the three Re_m cases studied.

Both mono-frequency and multi-frequency responses are noted along the cylinder span in the in-line and cross-flow directions; each excited frequency is generally associated with a single structural wavenumber. The structural vibration frequencies differ substantially from the natural frequencies modified by considering an added mass coefficient of 1; this emphasizes the variability of the added mass coefficient.

A ratio of approximately 2 can be identified between the in-line and cross-flow vibration frequencies, leading to 'figure-eight' trajectories in the (x, y) planes. Near the high-oncoming-velocity end ($z = 0$), where the standing-wave character of the structural response dominates, a region of alternating clockwise and counter-clockwise orbits was identified. Outside this region, the phase difference between the in-line and the cross-flow vibrations exhibits a zigzagging spanwise pattern.

For the linearly sheared current studied, the synchronization between vortex shedding and structural vibration, the lock-in condition, occurs in a region that corresponds at least to 30 % of the cylinder length, lying within the high-velocity zone. Observed discontinuities of the vortex shedding frequency along the cylinder span in the remaining, non-lock-in region, cause vortex-splitting events, that are required to ensure the continuity of the vortex filaments.

The principal new findings on the fluid–structure interaction mechanisms involved in the VIV of long flexible cylinders in shear flow are summarized as follows.

Wake patterns. Within both the lock-in and non-lock-in regions, mostly oblique vortex shedding is observed. The orientation of the travelling wave component of the structural vibration, from high- to low-velocity regions, follows the orientation of the oblique vortex rows. The non-lock-in region contains discontinuous cellular patterns, composed of spanwise cells of constant shedding frequency, similar to the case of a long stationary cylinder in shear flow. We find that the cell length is approximately equal to half the wavelength of the cross-flow structural vibration.

Orbital motion as it relates to lock-in/non-lock-in conditions. Lock-in versus non-lock-in conditions influence the phase angle between the in-line and cross-flow motions; we find mainly counter-clockwise orbits within the lock-in region. The flow provides energy to the structure within the lock-in region, while it damps the structural vibrations in the non-lock-in region. We find, however, that the energy input is not uniform across the entire lock-in region, due to the observed changes from counter-clockwise to clockwise structural orbits, which cause a significant reduction in the force coefficient in phase with the velocity.

Mechanisms of multi-frequency vibration. We find that multi-frequency responses consist of several locally and instantaneously mono-frequency events. The overall multi-frequency character is due to a temporal drift of the excited frequency, which switches smoothly among the predominant frequencies. In the lock-in region, at any given spanwise location, the wake is synchronized with a single vibration frequency, that also corresponds to the locally predominant frequency of the structural response. As a consequence, the lock-in condition does not occur continuously as a function of time. In addition, the spanwise lock-in pattern is discontinuous and thus multiple vortex splitting events occur. As in the mono-frequency case, the flow excites the structure under the lock-in condition, supplying energy mainly at a single frequency for a given spanwise location, even though the cylinder may exhibit, overall, a multi-frequency vibration.

The results found herein have implications for applications, especially in the field of marine structures, such as risers and cables in sheared ocean currents. The Reynolds numbers in the present study were chosen to reach the regime of turbulent wake, as this ensures capturing principal mechanisms of vortex formation. Although the Reynolds numbers are relatively low compared to full-scale applications, experimental and field studies carried out at much higher Reynolds numbers (Lie & Kaasen 2006; Vandiver *et al.* 2009; Dahl *et al.* 2010) have provided evidence that important features of the free vibrations described here, such as the possibility of multi-frequency response and the preferential in-line/cross-flow motion synchronization patterns, are also observed at high Reynolds numbers. A major finding in this study is that when multi-frequency response occurs, the mechanism of excitation is that of locally mono-frequency excitation; this is expected to influence the semi-empirical modelling efforts to predict VIV, which are based on short-span rigid cylinder hydrodynamic results. As a consequence, the present results can provide insights for both the development of VIV suppression or control techniques and the elaboration of simplified low-order models for fatigue damage quantification and offshore structure design.

The authors wish to acknowledge support from the BP-MIT Major Projects Programme, monitored by M. Tognarelli and P. Beynet; and the Office of Naval

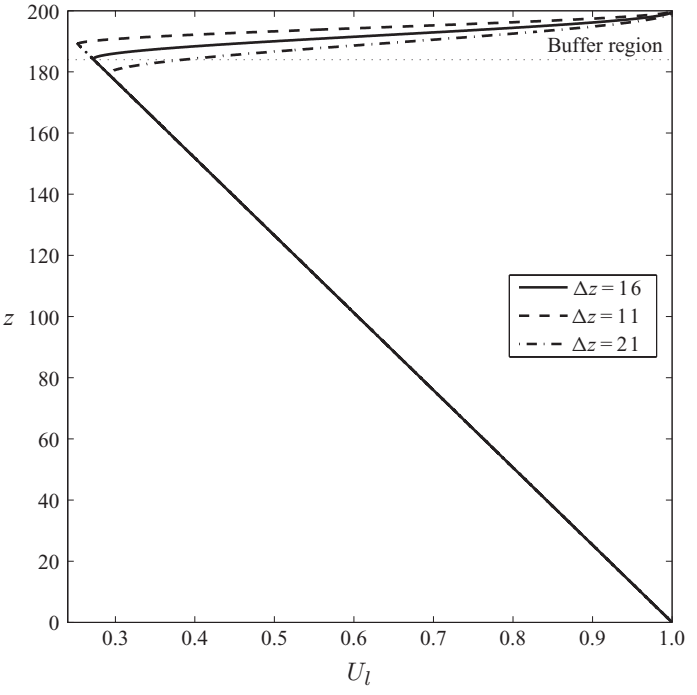

FIGURE 23. Oncoming flow velocity profile, including buffer regions of various sizes.

Research under grants N00014-07-1-0135 and N00014-07-1-0446, monitored by T. Swean, Jr.

Appendix A. Buffer region

A buffer region is used to enforce the spanwise periodicity of the inflow velocity profile. The buffer region inflow velocity profile is represented by a third-order polynomial that ensures continuity of the velocity profile and its slope. The size of the buffer region is chosen equal to 8 % of the cylinder length ($\Delta z = 16$), in agreement with the recommendations of Lucor *et al.* (2006). To quantify the influence of the buffer region on the rest of the domain, two additional simulations with $\Delta z = 11$ and $\Delta z = 21$ have been performed, at $Re_m = 110$. The corresponding inflow velocity profiles are plotted in figure 23. A comparison of the time-averaged in-line bending and r.m.s. values of the structure displacements, force coefficients and cross-flow component of the flow velocity in the wake, for the different buffer region sizes, is presented in figure 24. The relative difference in the vibration frequencies is smaller than 0.5 % between $\Delta z = 11$ and $\Delta z = 21$ cases. It appears that the buffer region size has a negligible impact on the flow and structural vibrations in the rest of the domain, as long as it remains small compared to the cylinder length.

In addition, the vibrations observed in the present work are similar to those measured experimentally by Trim *et al.* (2005), Lie & Kaasen (2006) and Vandiver *et al.* (2009), for example, which corroborates the absence of spurious effects due to the buffer region in the simulations.

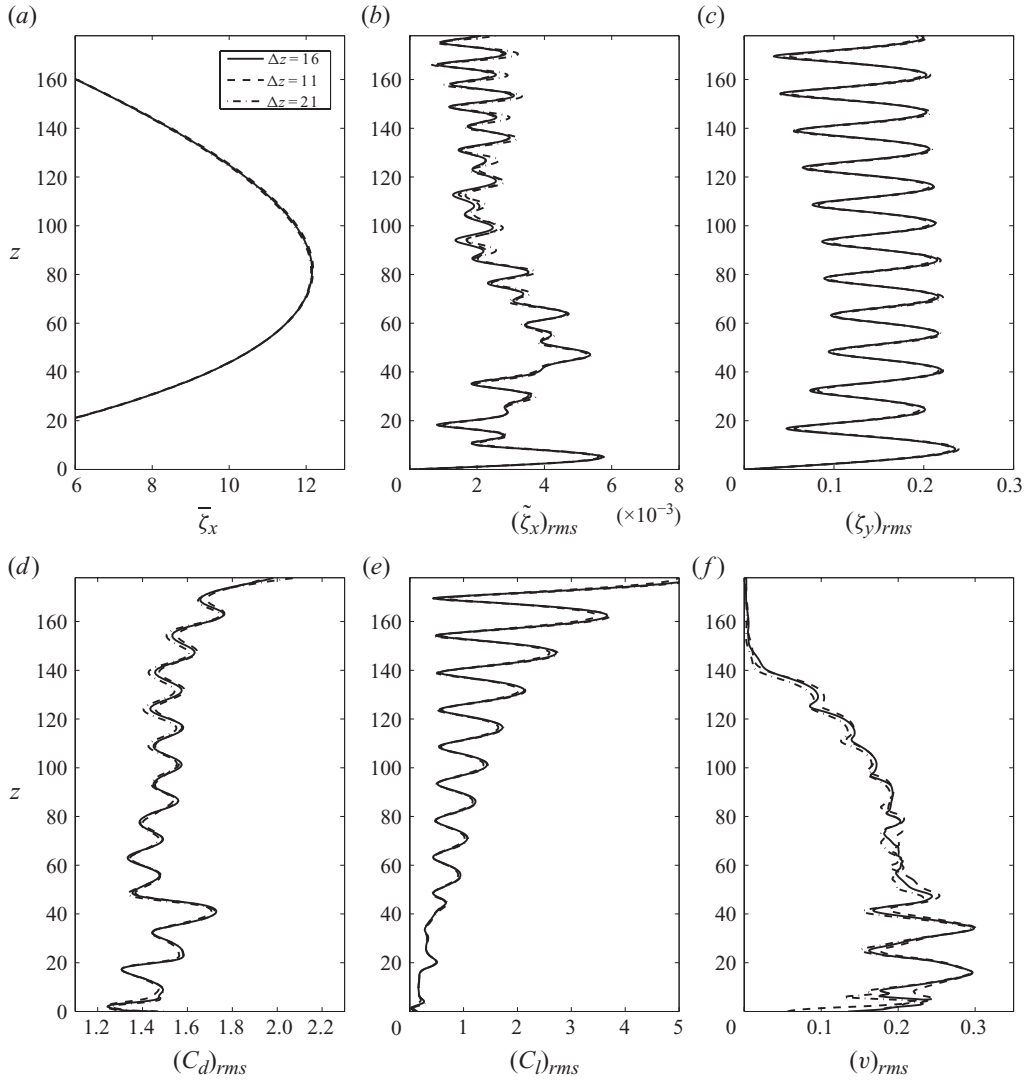

FIGURE 24. Impact of the buffer region size on the: (*a*) time-averaged in-line displacement, and r.m.s. values of the (*b*) in-line displacement fluctuation, (*c*) cross-flow displacement, (*d*) drag coefficient, (*e*) lift coefficient and (*f*) cross-flow component of the flow velocity at $(x, y) = (20, 0)$, along the cylinder span, at $Re_m = 110$.

Appendix B. Computational resources

Simulation runs have been performed on a Cray XT5 (Navy DoD Supercomputing Resource Center – Navy DSRC) and a Cray XT4 (Engineer Research and Development Center – ERDC), using one core per Fourier mode. Simulation at $Re_m = 1\,100$ was conducted on 512 cores and took approximately 3 s per time step. In this case, a non-dimensional time step of 0.0005 was considered, leading to approximately 13 000 time steps per cross-flow vibration cycle.

The typical integration time interval is approximately 600 convective time units, including approximately 300 time units of initial transient and 300 time units of data

sampling. Data sampling is started after convergence of the time-averaged in-line displacement of the cylinder.

REFERENCES

Bearman, P. W. 1984 Vortex shedding from oscillating bluff bodies. *Annu. Rev. Fluid Mech.* **16**, 195–222.

Boashash, B. 2003 *Time Frequency Signal Analysis and Processing: A Comprehensive Reference*, 1st edn. Elsevier.

Braza, M., Faghani, D. & Persillon, H. 2001 Successive stages and the role of natural vortex dislocations in three-dimensional wake transition. *J. Fluid Mech.* **439**, 1–41.

Brika, D. & Laneville, A. 1993 Vortex-induced vibrations of a long flexible circular cylinder. *J. Fluid Mech.* **250**, 481–508.

Carberry, J., Sheridan, J. & Rockwell, D. 2005 Controlled oscillations of a cylinder: forces and wake modes. *J. Fluid Mech.* **538**, 31–69.

Chaplin, J. R., Bearman, P. W., Huera-Huarte, F. J. & Pattenden, R. J. 2005 Laboratory measurements of vortex-induced vibrations of a vertical tension riser in a stepped current. *J. Fluids Struct.* **21**, 3–24.

Dahl, J. M., Hover, F. S., Triantafyllou, M. S., Dong, S. & Karniadakis, G. E. 2007 Resonant vibrations of bluff bodies cause multivortex shedding and high frequency forces. *Phys. Rev. Lett.* **99**, 144503.

Dahl, J. M., Hover, F. S., Triantafyllou, M. S. & Oakley, O. H. 2010 Dual resonance in vortex-induced vibrations at subcritical and supercritical Reynolds numbers. *J. Fluid Mech.* **643**, 395–424.

Evangelinos, C. & Karniadakis, G. E. 1999 Dynamics and flow structures in the turbulent wake of rigid and flexible cylinders subject to vortex-induced vibrations. *J. Fluid Mech.* **400**, 91–124.

Facchinetti, M. L., de Langre, E. & Biolley, F. 2004 Vortex-induced travelling waves along a cable. *Eur. J. Mech.* B/*Fluids* **23**, 199–208.

Flemming, F. & Williamson, C. H. K. 2005 Vortex-induced vibrations of a pivoted cylinder. *J. Fluid Mech.* **522**, 215–252.

Gaster, M. 1969 Vortex shedding from slender cones at low Reynolds numbers. *J. Fluid Mech.* **38**, 565–576.

Gaster, M. 1971 Vortex shedding from circular cylinders at low Reynolds numbers. *J. Fluid Mech.* **46**, 749–756.

Griffin, O. M. 1985 Vortex shedding from bluff bodies in a shear flow: a review. *J. Fluids Engng* **107**, 298–306.

Hover, F. S., Techet, A. H. & Triantafyllou, M. S. 1998 Forces on oscillating uniform and tapered cylinders in crossflow. *J. Fluid Mech.* **363**, 97–114.

Huera-Huarte, F. J. & Bearman, P. W. 2009*a* Wake structures and vortex-induced vibrations of a long flexible cylinder. Part 1. Dynamic response. *J. Fluids Struct.* **25**, 969–990.

Huera-Huarte, F. J. & Bearman, P. W. 2009*b* Wake structures and vortex-induced vibrations of a long flexible cylinder. Part 2: Drag coefficients and vortex modes. *J. Fluids Struct.* **25**, 991–1006.

Huera-Huarte, F. J., Bearman, P. W. & Chaplin, J. R. 2006 On the force distribution along the axis of a flexible circular cylinder undergoing multi-mode vortex-induced vibrations. *J. Fluids Struct.* **22**, 897–903.

Jaiswal, V. & Vandiver, J. K. 2007 VIV response prediction for long risers with variable damping. In *Proceedings of the 26th International Conference on Offshore Mechanics and Arctic Engineering* (OMAE2007-29353).

Jauvtis, N. & Williamson, C. H. K. 2004 The effect of two degrees of freedom on vortex-induced vibration at low mass and damping. *J. Fluid Mech.* **509**, 23–62.

Jeon, D. & Gharib, M. 2001 On circular cylinders undergoing two-degree-of-freedom forced motions. *J. Fluids Struct.* **15**, 533–541.

Kappler, M., Rodi, W., Szepessy, S. & Badran, O. 2005 Experiments on the flow past long circular cylinders in a shear flow. *Exp. Fluids* **38**, 269–284.

Karniadakis, G. E. & Sherwin, S. 1999 *Spectral/hp Element Methods for CFD*, 1st edn. Oxford University Press.

Lie, H. & Kaasen, K. E. 2006 Modal analysis of measurements from a large-scale VIV model test of a riser in linearly sheared flow. *J. Fluids Struct.* **22**, 557–575.

Lucor, D. 2004 Generalized polynomial chaos: applications to random oscillators and flowstructure interactions. PhD Thesis, Brown University.

Lucor, D., Imas, L. & Karniadakis, G. E. 2001 Vortex dislocations and force distribution of long flexible cylinders subjected to sheared flows. *J. Fluids Struct.* **15**, 641–650.

Lucor, D., Mukundan, H. & Triantafyllou, M. S. 2006 Riser modal identification in CFD and full-scale experiments. *J. Fluids Struct.* **22**, 905–917.

Mathelin, L. & de Langre, E. 2005 Vortex-induced vibrations and waves under shear flow with a wake oscillator model. *Eur. J. Mech.* B/*Fluids* **24**, 478–490.

Modarres-Sadeghi, Y., Mukundan, H., Dahl, J. M., Hover, F. S. & Triantafyllou, M. S. 2010 The effect of higher harmonic forces on fatigue life of marine risers. *J. Sound Vib.* **329**, 43–55.

Mukhopadhyay, A., Venugopal, P. & Vanka, S. P. 1999 Numerical study of vortex shedding from a circular cylinder in linear shear flow. *J. Fluids Engng* **121**, 460–468.

Newman, D. J. & Karniadakis, G. E. 1997 A direct numerical simulation study of flow past a freely vibrating cable. *J. Fluid Mech.* **344**, 95–136.

Noack, B. R., Ohle, F. & Eckelmann, H. 1991 On cell formation in vortex streets. *J. Fluid Mech.* **227**, 293–308.

Peltzer, R. D. & Rooney, D. M. 1985 Vortex shedding in a linear shear flow from a vibrating marine cable with attached bluff bodies. *J. Fluids Engng* **107**, 61–66.

Persillon, H. & Braza, M. 1998 Physical analysis of the transition to turbulence in the wake of a circular cylinder by three-dimensional Navier–Stokes simulation. *J. Fluid Mech.* **365**, 23–88.

Piccirillo, P. S. & Van Atta, C. W. 1993 An experimental study of vortex shedding behind linearly tapered cylinders at low Reynolds number. *J. Fluid Mech.* **246**, 163–195.

Sarpkaya, T. 1995 Hydrodynamic damping, flow-induced oscillations, and biharmonic response. *J. Offshore Mech. Arctic Engng* **117**, 232–238.

Sarpkaya, T. 2004 A critical review of the intrinsic nature of vortex-induced vibrations. *J. Fluids Struct.* **19**, 389–447.

Stansby, P. K. 1976 The locking-on of vortex shedding due to the cross-stream vibration of circular cylinders in uniform and shear flows. *J. Fluid Mech.* **74**, 641–665.

Techet, A. H., Hover, F. S. & Triantafyllou, M. S. 1998 Vortical patterns behind a tapered cylinder oscillating transversely to a uniform flow. *J. Fluid Mech.* **363**, 79–96.

Trim, A. D., Braaten, H., Lie, H. & Tognarelli, M. A. 2005 Experimental investigation of vortex-induced vibration of long marine risers. *J. Fluids Struct.* **21**, 335–361.

Vandiver, J. K., Jaiswal, V. & Jhingran, V. 2009 Insights on vortex-induced, traveling waves on long risers. *J. Fluids Struct.* **25**, 641–653.

Violette, R., de Langre, E. & Szydlowski, J. 2007 Computation of vortex-induced vibrations of long structures using a wake oscillator model: comparison with DNS and experiments. *Comput. Struct.* **85**, 1134–1141.

Williamson, C. H. K. 1989 Oblique and parallel modes of vortex shedding in the wake of a circular cylinder at low Reynolds numbers. *J. Fluid Mech.* **206**, 579–627.

Williamson, C. H. K. 1992 The natural and forced formation of spot-like 'vortex dislocations' in the transition of a wake. *J. Fluid Mech.* **243**, 393–441.

Williamson, C. H. K. & Govardhan, R. 2004 Vortex-induced vibrations. *Annu. Rev. Fluid Mech.* **36**, 413–455.

Williamson, C. H. K. & Roshko, A. 1988 Vortex formation in the wake of an oscillating cylinder. *J. Fluids Struct.* **2**, 355–381.

Zhang, H.-Q., Fey, U., Noack, B. R., Konig, M. & Eckelmann, H. 1995 On the transition of the cylinder wake. *Phys. Fluids* **7**, 779–794.